Influence of current pulse profile on metal transfer in pulsed gas metal arc welding

by

Emanuel Bruno Ferreira Dos Santos

A thesis
presented to the University of Waterloo
in fulfillment of the
thesis requirement for the degree of
Master of Applied Science
in
Mechanical and Mechatronics Engineering

Waterloo, Ontario, Canada, 2017

This thesis consists of material all of which I authored or co-authored: see Statement of Contributions included in the thesis. This is a true copy of the thesis, including any required final revisions, as accepted by my examiners.

I understand that my thesis may be made electronically available to the public.

Statement of contribution

Section 4.2 of Chapter 4 has been incorporated within a paper that has been submitted for publication. The paper is co-authored by myself, Mrs. Kuroiwa, Mr. Ferreira, Mr. Pistor, and my supervisor (Dr. Gerlich). I developed and documented the methodology, performed the experiments, analyzed the results and wrote the manuscript. Mrs. Kuroiwa and Mr. Ferreira collected the experimental data. Mr. Pistor and Dr. Gerlich assisted with the writing of the paper.

Section 5.1 of Chapter 5 consists of a paper that was co-authored by myself, Mr. Pistor, and my supervisor (Dr. Gerlich). I developed and documented the methodology, performed the experiments, collected and analyzed the results, and wrote the manuscript. Mr. Pistor and Dr. Gerlich assisted me with experimental planning and with the writing of the paper.

Section 5.2 of Chapter 5 consists of a paper that was co-authored by myself, Mr. Midawi, and my supervisor (Dr. Gerlich). I developed and documented the methodology, performed the experiments, collected and analyzed the results, and wrote the manuscript. Mr. Midawi helped with collected and analyzed the results and writing the paper. Mr. Pistor and Dr. Gerlich assisted me with experimental planning and with the writing of the paper.

Chapter 6 consists of a paper that was co-authored by myself, Mr. Pistor, and my supervisor (Dr. Gerlich). I developed and documented the methodology, performed the experiments, analyzed the results and wrote the manuscript. Mr. Pistor and Dr. Gerlich assisted with the writing of the paper.

Abstract

The increase in the requirements of safety and reliability demanded from the normalization institutes by the issue of normalizing standards, led to the need of the development of materials of superior properties. Owing to the development of metallurgy, the development of materials with extremely high values of strength and toughness was made possible. However, employing these materials in industrial applications is limited by the deterioration of their properties after the material is processed using techniques such as welding.

To cope with this challenge, several welding process have been developed. One of these processes is the pulse gas metal arc welding (GMAW-P), in which the arc current is periodically pulsed in order to achieve metal transfer and effectively join the material being dealt with, and this decrease the energy input to the base metal. Due to the advance of electronics and transistor technology there are a large number of current pulse profiles commercially available, with different degrees of complexity, designed for specific applications. Determining the balance between the complexity and benefits for the various pulse profiles and process modifications available is the main motivation for the research presented in this thesis. Specifically, the metal transfer of two commercially available current profiles was studied using high-speed imaging and high speed data acquisition of the electrical signal during welding, for different welding conditions. The results showed that the mode of metal transfer differs for the investigated profiles and that for the same pulse profile, as the pulse parameters are modified the metal and heat transfer changes, altering weld bead features such cross-sectional area and penetration.

Acknowledgements

First and foremost, I would like to thank my supervisor Prof. Adrian P. Gerlich for giving me the opportunity to come to the University of Waterloo for my masters studies. Thank you for the technical discussions, sharing your experience. You gave to me all the support and freedom I would ever need to conduct the work toward this master thesis. Thank you for all the opportunities, please know that I am truly grateful to all the opportunities that I have had due to your support.

To all the CAMJ group members, in special those in the Pipeline Research Subgroup, Abdalbaset Midawi, Arshad Haroni, Nazmul Huda, Michael Both, Chris Gobbi, Yuji Kisaka, Luqman Shah, Rangarajan Padmanabhan, Rafael Ribeiro and RahulRam Chandrasekaran. Thank you for everything, in fact I feel privileged to have had the opportunity of share space, discussions and contribution with you all in a daily basis.

The support from the Faculty of Engineering technical staff:

- Neil Griffet, the electronics technician from the Department of Mechanical and Mechatronics Engineering, for his support with setting up the data acquisition system, which was of fundamental importance for the development of this work.
- Mark Griffet, the materials laboratory technologist for helping me with his long experience, counseling and providing me ideas with simple ideas, yet really effective, for the solution of problems faced in a daily basis when performing experiments. Or sometimes pointing me for solution when I though to have exhausted all my problem solve skills resource.
- To the Engineering Machine Shop staff Jorge Cruz, Graeme Adair, Phil Laycock and Andrew Urschel for their promptitude to help whenever I needed, and sharing their experience with me. What I learned from all of you, I truly consider to tbe invaluable.

I am grateful to professors Carolyn M. Hansson, Michael Mayer, Shahrzad Esmaeili and Charles C.F. Kwan, for giving me the opportunity of assist then in teaching undergraduate

courses, as a Teaching Assistant. More than helping with my monthly expenses, this experience gave the opportunity of develop and practice my teaching skills, and gave the the taste of what is it like to be on the other side of the professor and student relationship. It was a great learning experience, much more learning than teaching.

I am deeply grateful to all the mentors I had throughout my student experience, from "Tia Lola", who taught me how to write and elementary math operations, through high school, to my professors in university during my undergraduate studies. Without the support I have had of each of you, I would not have ever accomplished any of what I have done.

In the name of Rafael Pantaroto and his family, I would like to thank you the support of all my friends, for their encouraging words, which certainly helped throughout the journey.

Finally, the highest gratitude goes to my parents Geraldo (Negão) and Iraceles (Célia), for doing everything they could to support me on working toward my goals, I know you both did everything you could to support, sometimes even doing what you thought you could not do. I cannot put into words how grateful I am to you both. Thank you to my sister Eluana Bruna. Rafael Rendel, who I have as a brother, for his support to my parents when I was not able to the around. Last but not least, to my girlfriend Deanna Ritchie, who unconditionally celebrated 'good' and made me feel good in the 'bad' days. You know how much you mean to me amor. Thank you!

Emanuel B. F. Dos Santos *Waterloo, ON, Canada, 2017*

Dedication

I would like to dedicate this work to my loved parents, Geraldo and Iraceles, to my sister Eluana Bruna, to my brother Rafael Rendel, to my friend Raphael Pantaroto and his family. I also would like to dedicate it to all my professors, who dedicated their time to guide me in my life and transformed it.

Table of Contents

List of Tables

List of Figures

You can achieve anything you want in life,
given you make your goals stronger than the
difficulties you may encounter.

Emanuel B. F. Dos Santos

Chapter 1

Introduction

In the manufacturing of any large structure, such as ships, airplanes, off-shore platforms, numerous cross-sections have to be joined together. For instance, Fig. 1.1 shows the first floating liquefied natural gas ship, which will be 488 m (1,600 feet) long, 74m (240 feet) wide and weigh around 600,000 tonnes [11]. In order to build such a large structure, plates of steel have to be joined to form blocks and the assembly of several blocks will turn into the ship hull. The plates of steel have to be joined together, either due to the impossibility of producing the required metal in such larger dimensions, or the need of using different materials, or both. When the material to be joined is a metal, welding is one of the most used joining process. Several welding processes are available, and the application of a particular process will depend on the specific characteristics of each project.

Regarding on-shore exploration and transportation of energy, pipelines are most used, either for transportation of crude oil for refineries, or for the distribution to the end consumer. Those pipelines can extend over thousands of kilometres. In Canada, according to Canadian Energy Pipeline Association (CEPA), about 119,000 kilometres of pipelines are operated by pipeline companies [12]. Pipelines are mostly built from individual steel pipe section typically 12 m long, and in order to increase the transportation capacity, higher strength steels are being developed to be employed in the construction of the new pipelines [13]. In addition to the increased transportation capacity, higher strength steels would allow for reduction of the wall thickness, which in turn will have a consequence in

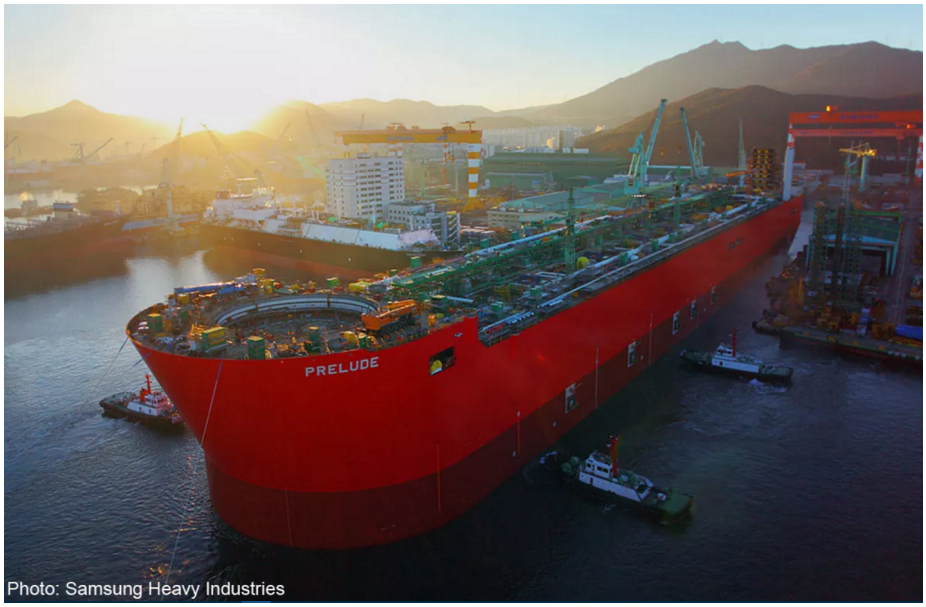

Figure 1.1: The world's first floating liquefied natural gas facility [1].

reducing construction cost due to transportation of pipes and welding during the construction phase.

Although there has even been reported in the literature high strength steels with Charpy V-notch impact energy of 400-450 J combined with a tensile strength as high as 1.2 GPa [14], pipelines are mostly built using the so-called high strength low alloy (HSLA) steels. The steels for the construction of such high capacity pipelines are produced in industrial scale, as for instance the thermo-mechanical controlled and processed steels with yield strengths of up to 830 MPa (X120) and impact toughness of 210 J at -30 °C [15–17]. However, due to the intrinsic chemical composition of these steels and how they are produced, they have increased hardenability and refined microstructure, and once welding is performed, the degradation of the steel properties at the heat affected zone (HAZ) is inevitable. Therefore, the wide application of such high strength steel in the construction of the new generation of higher capacity and safer pipelines is dependent on the development of welding technologies that would allow the joining of these steels such that the deterioration of the steel properties at the HAZ is minimized.

The gas metal arc welding (GMAW) process is widely used in the construction of pipelines. Due to the potentially excessive heat input, the degradation of the HAZ is a concern. Alternative welding processes have been developed and are being studied in order to employ them for joining of these steels. Friction stir welding (FSW) is one example of the new welding process developed [18] and that can successfully join the higher grade pipeline steels with superior properties [19], however it is not yet economically feasible due to the high cost of the tool materials required for welding steels [20].

Despite all the development of alternative welding process, GMAW is still the most widely used welding process due to it productivity and versatility. Several modifications proposed to this process have emerged, such that the heat input imposed to the base metal could be reduced. One of these modifications was proposed in 1960's [21, 22] and consists of using pulsed current waveform instead, transferring the metal from the welding wire the welding pool in a controlled manner. Since the invention of pulsed gas metal arc welding (GMAW-P), the advance of electronics and transistor technology allowed the various welding power supply manufactures to produce a large number of current pulse profiles, with different degrees of complexity, for the most diverse applications. In terms of current profile shape, they range from a simple square wave [22], to more complex shapes such as the Surface Tension Transfer (STT) [23] and Cold Metal Transfer (CMT) [24] controlled metal transfer processes.

The weld joint performance is strongly dependent on the joint geometry and microstructure of the resulting weld metal and HAZ. An in GMAW welding, the way the weld metal is transferred from the welding wire to the weld pool will determine the mass and heat transfer to the base metal and the final bead geometry, and consequently the joint performance.

1.1 Motivation

Given the variety of current pulse profiles available, and the dependence of joint performance on the metal transfer phenomenon, one question comes to mind: what is the influence on current pulse profile on metal transfer? Are the benefits from the features

included in the current pulse profiles worth the added complexity involved in the design of the power supplies? The answers to these questions are the main source of motivation for the research presented in this dissertation.

1.2 Objective

1.2.1 Main objective

In this work, the metal transfer for two current pulse profiles will be investigated. One pulse profile has a nearly square shape, the other one has an exponential increase from background to peak current and then a long tail decay from peak to background current as a result of differences in the power supply circuit design. Both of these profiles are commercially available, and this work aims to identify the differences in metal transfer that would lead one to use the square wave pulse profile instead of that of a gradual transition and vice-versa.

1.2.2 Specific objectives

In order to achieve the main objective of this research, the following specific objectives will be tackled:

- Identify pulse parameters, for which the metal transfer occurs in the one-droplet-per-pulse transfer mode, for both profiles;
- Setup a high-speed data acquisition (DAQ) system to monitor the torch voltage and current during welding;
- Setup a high-speed camera, with the appropriated filters, to monitor droplet formation and detachment, and visualization of arc phenomenon of the different regions of the electric arc;

- Synchronize the DAQ system to the high-speed camera, and correlate the changes in electrical signals to droplet formation and detachment, and arc phenomenon;
- Correlate bead geometry to metal transfer. This will be done by measuring droplet speed and calculate the contribution of droplet momentum to bead penetration.

Chapter 2

Literature review

2.1 Gas metal arc welding (GMAW)

Gas metal arc welding (GMAW) is a welding process, in which a continuously fed wire is melted by an electric arc established between the tip of the wire and the workpiece. The invention of the GMAW process dates back to the first half of the 20th century, when on December 26, 1924, Peter P. Alexander from the General Electric Company filed a patent named "*Method and apparatus for electric arc welding*" [2], in which a process similar to what we know today as the GMAW process was described as the invention. In Figure 2.1 the illustration of the GMAW process described in the patent is shown.

Since its invention more than seven decades ago, the GMAW process has been the subject of numerous studies. Some of these studies were fundamental to the understanding of the physics of the process in terms of the mechanism by which metal transfer occurs [25, 26]. The understanding of the process allowed further development of the technique, and today the process is used extensively in the manufacturing industry due to its productivity and versatility. Despite all the development achieved, the advent of new materials drives the need of further development of this welding process, such that its productivity capability could be maintained or increased, and at the same time that the amount of heat transferred to the materials being joined is reduced. This still poses a challenge and several process modifications have been proposed and are currently still widely studied [27–29].

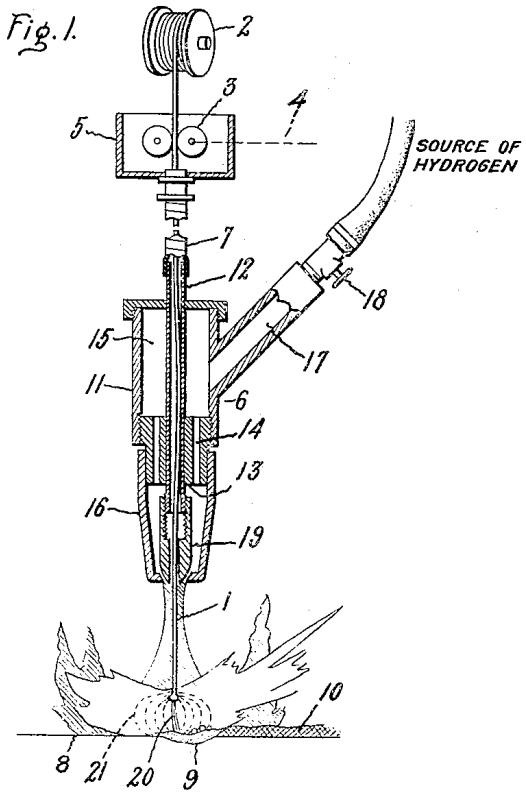

Figure 2.1: Schematic of the GMAW process in the patent filed in 1924 by Peter P. Alexander [2].

2.2 Metal transfer in GMAW

The strength of the final joint will depend on the weld geometry and microstructure [16], and these will depend on the heat and mass transfer phenomenon taking place during droplet transfer from the electrode to the weld pool [30, 10, 31–33, 9, 34–37], which are controlled by the welding parameters used [38–43]. Given the importance of metal transfer on the performance of the weld joint, the following subsection aims to review the forces acting on the metal transfer from the wire electrode to the workpiece (subsection 2.2.1), and then the observed metal transfer modes will be summarized (subsection 2.2.2). In Figure 2.2 the schematic of metal transfer in GMAW shows the droplet travelling through

the arc placed in an x-y coordinate system.

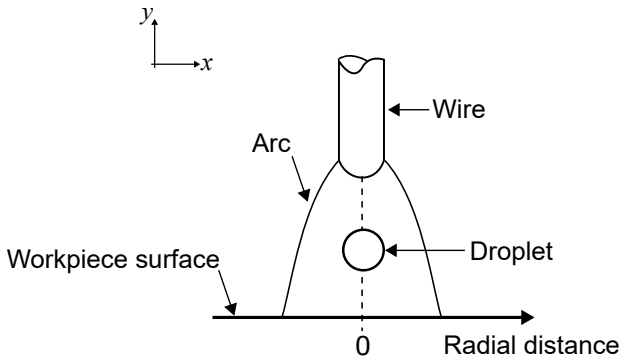

Figure 2.2: Diagram of metal transfer in GMAW and coordinate system.

2.2.1 Forces acting on metal transfer

One of the major forces acting on droplet formation and transfer, is the direct electromagnetic force due to the current flow through the forming droplet. The axial component of this force (acting on y-direction in Figure 2.2) help in droplet detachment and its magnitude is calculated by Equation 2.1,

$$F_{\text{em}} = \frac{\mu_0 I^2}{4\pi}\psi(s) \tag{2.1}$$

where, μ_0 is the magnetic permeability, I is the current flowing through the droplet, and $\psi(s)$ is a shape factor dependent on droplet size and shape, and how the current emerges from the forming droplet [25, 26].

The passage of current through the molten metal at the forming droplet induces fluid flow within it [32, 44], and this generates a momentum flux towards the electrode tip (y-direction in Figure 2.2), which then accelerates the droplet by conservation of momentum. This force increases with current according to Equation 2.2

$$F_{\text{mf}} = \frac{\mu_0}{4\pi}\left[\left(\frac{I}{\alpha}\right)^2 - I_d^2\right] \tag{2.2}$$

where α is the ratio between droplet and wire diameters, and I_d is the current flowing through the droplet tip. The force due to flow developed inside the droplet was derived by Arif et al. [3, 45], who demonstrated that the magnitude of the force due to momentum flux can be as high as that of electromagnetic force as the welding current increases, as shown in Figure 2.3 for a steel wire of 1.2 mm diameter. They found that the force due to momentum flux increases with current, exceeding the electromagnetic force at a current of approximately 220 A, which in this case corresponds to the transition current where metal transfer changes from globular to streaming spray.

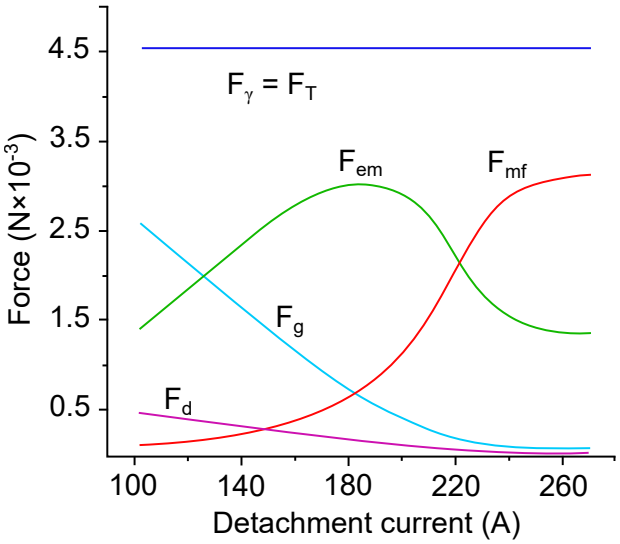

Figure 2.3: Variation of the magnitude of the forces acting on detaching droplet with welding current for a 1.2 mm steel welding wire. F_{T} is the total force acting on the droplet; F_{γ} the force due to surface tension; F_{em} the electromagnetic force; F_{mf} the force due to momentum flux; F_{d} the drag force and F_{g} the force due to gravity. Adapted from [3].

The forming droplet is not only under the influence of forces acting in favour of detachment, but also forces preventing detachment. One of these is the retaining force due to arc pressure, which is induced by the interaction of the current flowing through the arc and its own magnetic field [26]. The total axial force preventing droplet from detachment is given by Equation 2.3 [46].

$$F_{\mathrm{a}} = \frac{\mu_0 I^2}{8\pi} \tag{2.3}$$

Surface tension also exerts a retaining force during droplet formation and detachment, and its magnitude can be estimated according to Equation 2.4, where d is the diameter of the droplet and γ is the molten metal surface tension coefficient.

$$F_\gamma = \pi d\gamma \tag{2.4}$$

Once the droplet is detached, it will be further accelerated by the action of a drag force due to the axial flow in the arc plasma column. The axial arc plasma velocity, v_a, can be calculated by Equation 2.5 [46]

$$v_\mathrm{a} = \frac{3}{64}\frac{\mu_0 I^2}{\pi^2 r_r \eta} \tag{2.5}$$

where η is the dynamic viscosity of the arc plasma, and r_r is the distance from the arc axis.

The variation in axial pressure associated with this flow is given by Equation 2.6 [46], where l is the axial distance from the bottom of the forming droplet.

$$p_\mathrm{a} = \frac{3\mu_0 I^2}{64\pi^2 l^2} \tag{2.6}$$

The force and acceleration exerted on the droplet due to drag is obtained by Equation 2.7 and 2.8, where ρ_g is the shielding gas density and C_d is the drag coefficient.

$$F_\mathrm{d} = \frac{\pi}{2} 3 v^2 \rho_g r^2 C_d \tag{2.7}$$

$$a_\mathrm{d} = \frac{3}{8}\frac{v^2 \rho_g}{r \rho_m} C_d \tag{2.8}$$

Gravity also plays a role in droplet transfer, however for metal transfer occurring at high values of currents, the force due to gravitational acceleration, g, has a secondary effect on droplet velocity, when compared to the other forces playing a role, such as electromagnetic, arc pressure, plasma drag forces, and momentum conservation, as noted in Figure 2.3. In fact, droplet acceleration has been measured and it has been reported that the acceleration of droplets travelling through the arc can be up to 100 g [26, 47, 3, 46, 48, 49], hence proving

the secondary effect of gravity in droplet detachment at high current values.

2.2.2 Metal transfer modes

As exemplified in Figure 2.3, the magnitude of the forces acting on metal transfer changes depending on the value of the average welding current used, and this will promote metal transfer to occur in distinct modes [38, 39], each depending on the forces that predominat. Increasing the values of average current will promote a transition in metal transfer modes from short-circuiting, to globular, and then spray (projected, streaming or rotating) [50]. There may be conditions where, for a given welding current, more than one of these transfer modes can exist simultaneously, i.e., short-circuiting and globular, globular and spray. The occurrence of more than one metal transfer mode at once was termed by Scotti at al. as interchangeable metal transfer [51]. The following briefly summarizes transfer modes in terms of increasing welding current, which is normally proportional to wire feeding speed.

Short-circuiting transfer

Metal transfer by short-circuiting mode occurs at low welding current values, and the metal transfer occurs when the forming droplet touches the weld pool before detachment. In this transfer mode, surface tension is the force playing a role whether or not metal transfer occurs [52]. Although this transfer mode is achieved at low heat input values, it has the undesirable feature of spatter generation, which compromises the welding appearance, thus limiting the use of this transfer mode for some applications.

Globular transfer

Increasing welding current and/or welding voltage, to sufficient values to avoid short-circuiting, the droplet will form at the tip of the welding wire and then be transferred due to mostly the action of gravity and electromagnetic forces [25, 26]. To be called globular transfer mode, the droplets being transferred must have a diameter larger than the electrode, normally being 1.5 to 3 times the wire diameter, with droplet transfer rates typically below 10 droplets per second [51].

Spray transfer

With a further increase in welding current, the droplet diameter starts to decrease, and after a certain current value, it becomes smaller than the wire diameter, which characterizes the spray transfer. There is also a sudden increase in droplet transfer frequency, to values higher than 300 Hz [38, 39]. The current above which metal transfer takes place in spray mode is called transition current and its value depends on electrode material and diameter, and shielding gas used [47, 38, 39, 53, 54]. Spray transfer can occur in different modes, transitioning from projected, streaming and rotating spray transfer, with increasing of current [50]. Spray transfer is desirable due to the regularity of the transfer, low rates of spatter, high bead penetration and lower rate of fume formation compared the other modes [55].

The drawbacks are that in order to achieve spray transfer, pure argon or argon and oxygen gas mixture is required, and the average current value has to assume a minimum value, i.e. the transition current, and therefore it is not suitable for application such as the welding of thin plates, due to excessive distortion or burn-through of the sheet. Another disadvantage of spray transfer is that for some applications where heat input is a concern, such as the welding of high strength low alloy (HSLA) steels such as pipeline construction [16], this transfer mode can not be used. In welding of heat sensitive materials such as high strength steels, one technique used to reduce the amount of heat given to the base metal, hence the damage to the base metal microstructure adjacent to the weld, is to use narrow gap grooves. This would reduce the number of passes needed to complete the joint and consequently the overall amount of heat given to the base metal. One difficulty in narrow gap welding is the erosion of the groove sidewalls that occurs when long arcs are used. This sidewall erosion increases the chances of internal defects on the joint such as lack of fusion due to groove damage from long arcs [56]. Therefore, it is desirable to use welding parameters which lead to metal transfer with a small arc length, such as short circuit and globular transfer, and avoid use of long arc length when applying spray and stream transfer modes.

2.3 Pulsed gas metal arc welding (GMAW-P)

Another technique used to reduce the heat input to the base metal, while also avoiding spatter, is to use pulsed current instead of constant voltage power sources. This process is called pulsed gas metal arc welding (GMAW-P), and is widely employed in industry due to its advantages such as a controlled metal transfer in spray mode, at current values well below the transition current required to induce spray transfer when constant voltage GMAW is used. GMAW-P was first proposed in the 1960s, when an ideal square current was used to achieve a synthetic spray transfer with welding currents as low as 50 A, hence reducing the average current required to stable metal transfer [21]. Metal transfer in GMAW-P aims to achieve a controlled metal transfer in one droplet per pulse (ODPP) regime, and for that the process parameters have to meet certain conditions, which have been widely investigated [40, 57, 58].

Due to the advances in electronics, along with the development of high-speed inverter technology, several current pulse profiles are available from many welding power supply manufactures, ranging from the ideal square wave profile to more sophisticated complex waveforms [23, 59, 24]. Consequently, the different current profiles would provide metal transfer with different characteristics which can be advantageous depending on the application. However, one concern regarding pulse GMAW is the productivity associated with this process. Although pulsed GMAW can achieve higher deposition rates, there is still the need to increase productivity while maintaining heat input as low as possible.

2.4 Metal vapor and metal transfer in GMAW

The latest research on GMAW metal transfer has incorporated the influence of metal vapor on arc properties and investigated the implications of that on droplet formation and transfer. Using optical emission spectroscopy, Goecke [4] investigated the influence of small additions of nitrogen and oxygen to argon shielding gas when welding an aluminum - 5% magnesium electrode wire. In this study, it was first found that the temperature at the arc center axis was around 2,000 K lower than the maximum of 12,000 K at a distance of 2 mm

from the arc central axis [4]. This was verified for the different shielding gas mixtures used as shown in Figure 2.4. Goecke concluded that metal vapor flow in the center of the arc was the cause of the cooling of the plasma in center of the arc.

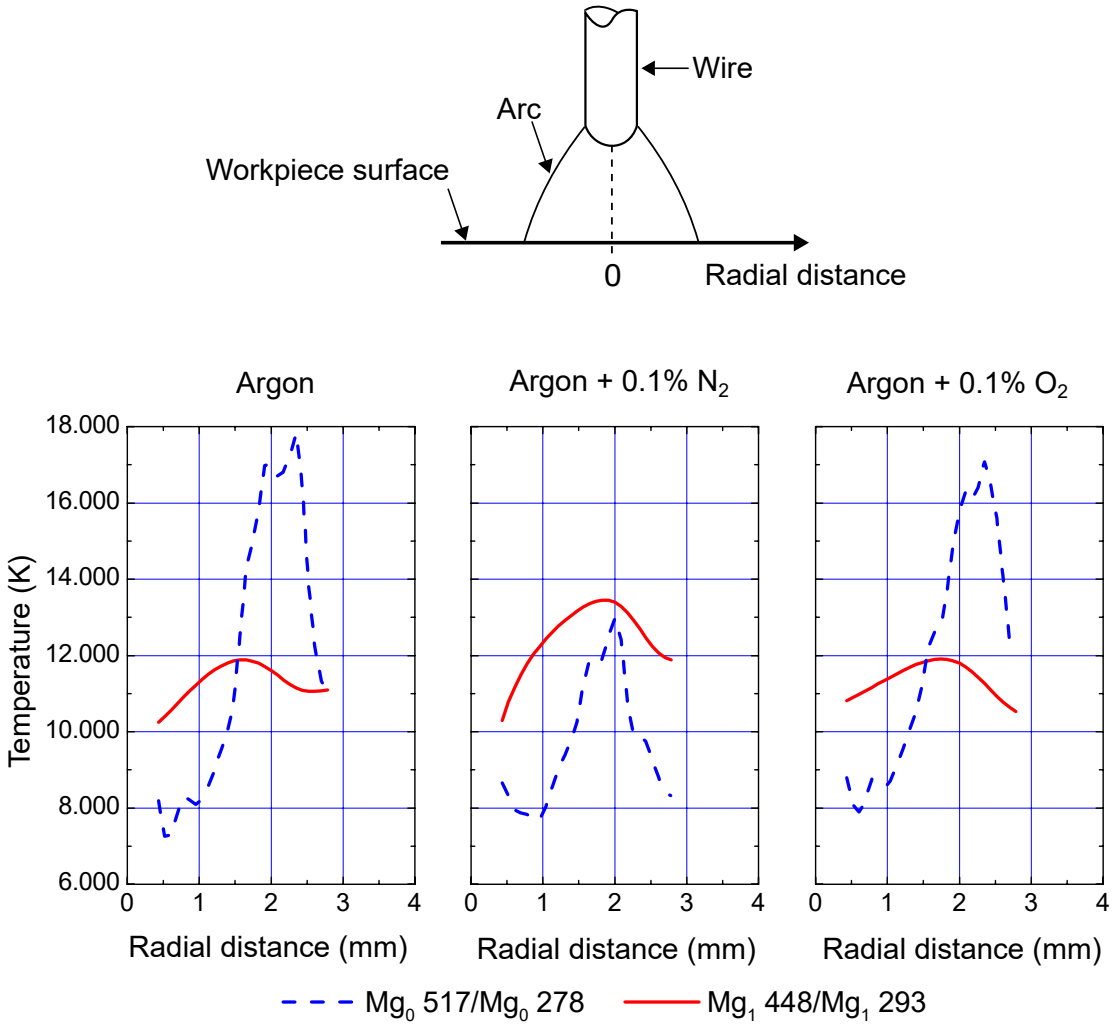

Figure 2.4: Radial temperature distribution calculated using relative method optical emission spectroscopy for different shielding gas mixtures and Al-5%Mg wire electrode of 1.0 mm diameter. Arc center axis is at 0 mm radial distance. Adapted from Goecke [4].

Later, Zielinsk et al. [60] used optical emission spectroscopy, to obtain electron densities and temperatures directly by measuring the Stark widths of the Ar I 695.5 nm and Fe I

538.3 nm spectral lines, for a steel electrode wire and different argon (Ar) - carbon dioxide (CO_2) shielding gas mixtures, i.e., including pure Ar, Ar - 5.4% CO_2 and Ar - 20.2% CO_2. It was also found that for pure argon and Ar-5.4 CO_2, the maximum temperature was not in the center of the arc.

After the works of Goecke [4] and Zielinsk et al. [60] much research has been aiming to investigate the role of metal vapor on arc properties and metal in constant voltage GMAW [61–63, 48, 64, 65, 7, 6] , GMAW-P [5, 66–68, 44, 69] and even more sophisticated process variations such as the controlled metal transfer process [70]. It was confirmed that there is an inner arc region, which consists of a high fraction of iron vapor, which is originally formed at the electrode tip due to overheating of the electrode and then dragged by the arc flow [60, 61, 71, 5, 63, 66]. Rouffet et al. [5] performed a spectroscopic investigation during the high-current phase of a pulsed GMAW process, Figure 2.5(a), and found that as the pulse progress into the high-current phase, the diameter of the iron core increases, Figure 2.5(b), and the peak temperature shifts further away from the centre of the arc, Figure 2.6(a). The measurements also revealed that as the pulse progresses the iron mole fraction increases, Figure 2.6(b).

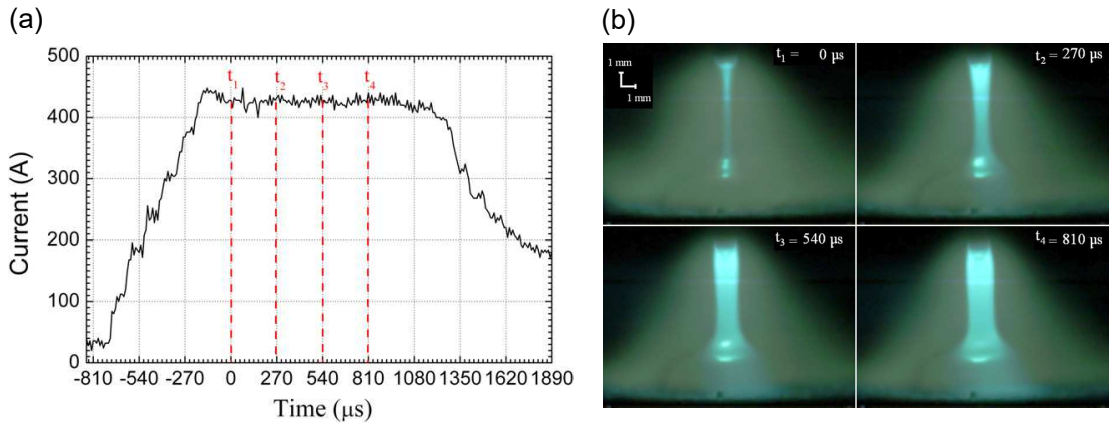

Figure 2.5: Metal vapour core evolution during current peak phase in GMAW-P [5].

The influence of metal vapour has been investigated numerically [61, 48, 63, 71, 64, 66, 6] and experimentally [5], and both results confirm an inner core composed of metal vapor, which enhances the plasma radiation loses [61, 64], hereby decreasing the plasma

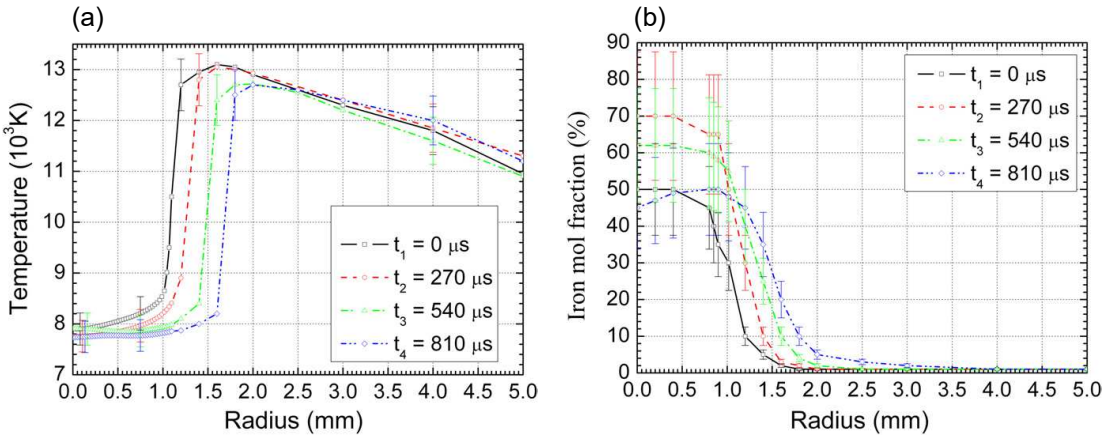

Figure 2.6: Temperature profiles of the plasma and (b) iron mol fraction at different times of the high-current phase [5].

temperature at central region of the arc, where a high fraction of iron metal vapor is present. A decrease in the plasma electrical conductivity is also observed as a consequence of the decrease in the plasma temperature [71, 6], which in turn alters the current path in the arc [44, 69].

Hertel et al. [44, 69] predicted that the decrease in plasma electrical conductivity at the bottom of the forming droplet, forces the arc to attach to the wire at a position closer to the contact tip instead of the wire tip or bottom of the forming droplet, hence reducing the amount of current flowing through the electrode necking region and forming droplet. This last point, regarding the change in arc attachment position, has not yet been experimentally observed. For pulsed GMAW, Boselli et al. [66] showed that the minimum in temperature at the center of the arc is only observed during the high current phase, whereas during the low current phase the temperature maximum returns to the central region of the arc at the bottom of the wire tip, as a consequence of the lower vaporization rates of the wire electrode due to lower arc temperatures [66, 68]. In a review of the effects of metal vapour in arc welding, Murphy [71] concluded that there is a large variation in the measured iron concentrations, raging from 1% [62] to 60% [5, 72], and even higher predicted concentrations by numerical modeling [64, 66, 44, 69, 6].

Valensi et al. [72] found that increasing the amount of CO_2 in the shielding gas sup-

presses the reduction in the arc core temperature in the globular transfer mode, agreeing with the first results of Zielinsk et al. [60], and further supported by recent results of Ogino et al. [6]. Furthermore, Ogino et al. [6] found that using Argon - 18% CO_2 shielding gas allows the current density to have its peak value distributed at the both of the droplet, compared to when pure argon is used, which then has a maximum current density at the sides of the forming droplet. This maximum current density at the bottom of the droplet increases the average arc pressure acting on the forming droplet, and hence explains why the transition current for metal transfer from globular to spray is higher when CO_2 is added to the shielding gas, Figure 2.7.

Given the importance of metal vapor on the understanding of the fundamentals of gas metal arc welding, alternative techniques have been developed to study these mechanisms during welding. One of these techniques involves high-speed cameras with a narrow band pass filter, for specific wavelength. In a recent work, Nomura and colleagues developed a tomographic spectroscopic technique using multiple CCD cameras, which allowed reconstruction of the arc structure, using for that narrow band pass filters for argon, Ar I, and iron, Fe I, spectral emission lines [7]. In Figure 2.8 and 2.9 the arc structure is shown for globular and spray metal transfer modes. Notice that when only the radiation from the argon is observed, the arc has a shape of a larger cone with diffuse boundaries, as evident in Figures 2.8(a) and 2.9(a), when compared to the arc core composed mostly of iron vapor which has sharper boundaries shown in Figures 2.8(b) and 2.9(b).

2.5 Metal transfer and bead geometry

Regarding the influence of metal transfer on the geometry of the forming bead, a relationship has been reported between the momentum of the impinging droplet and the bead penetration [8, 9]. Essers and Walter [8] reported that penetration increases with momentum rate, for different wire electrode diameters and polarities, Figure 2.10(a). The study concluded that the cross sectional area of weld penetration is mostly influenced by the heat content of the transferring droplet, while the depth of penetration is determined by the impact of the impinging droplet, namely the momentum rate of the droplet (mo-

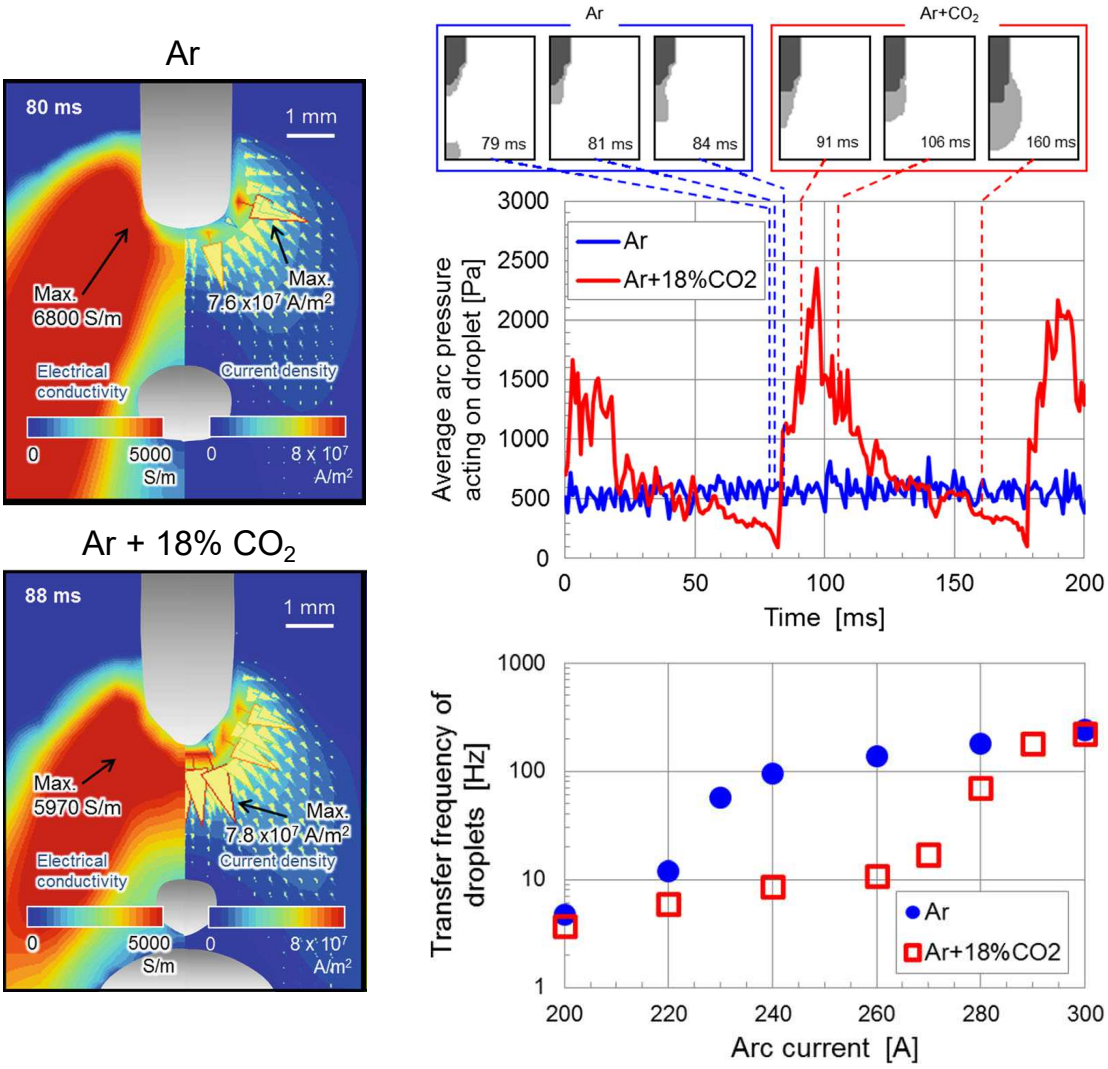

Figure 2.7: Influence of CO_2 content in shielding gas on metal vapor distribution and the implication of that on the electrical conductivity, current density distributions, average arc pressure acting on droplet and current for transition from globular to spray transfer modes. Adapted from Ogino et al. [6].

mentum multiplied by the frequency of droplet impingement). Scotti and Rodrigues [9] further investigated that relationship, but this time taking into account the arc length, Figure 2.10(b). The proportionality between momentum rate and bead penetration was also

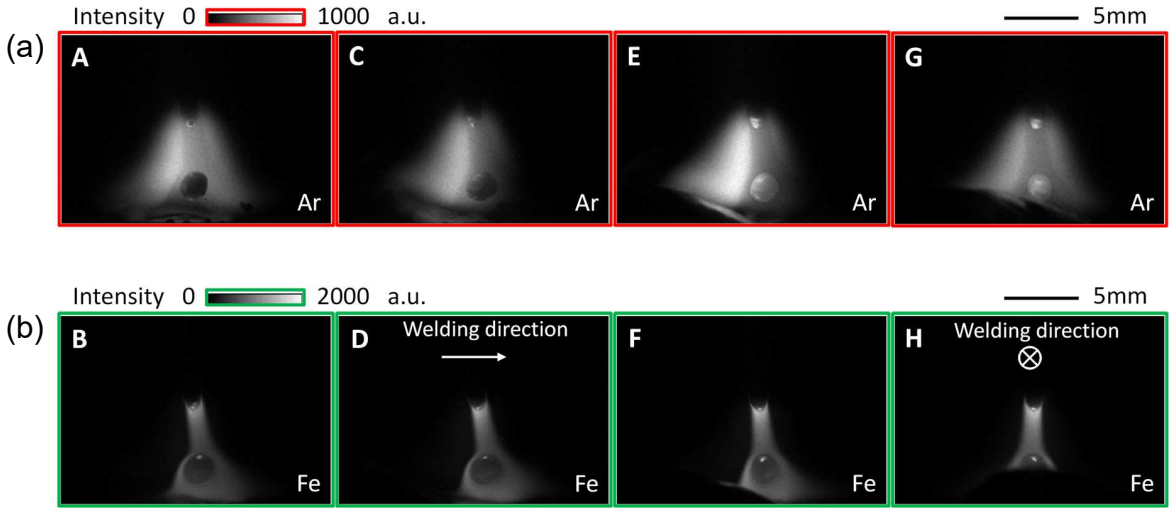

Figure 2.8: (a) argon and (b) iron dominated arc regions for globular transfer mode. Argon region imaged using Ar I spectral line (696.5 nm wavelength narrow band pass filter) and iron rich region imaged using Fe I spectral line (538.1 nm wavelength narrow band pass filter). Adapted from Namura et al. [7].

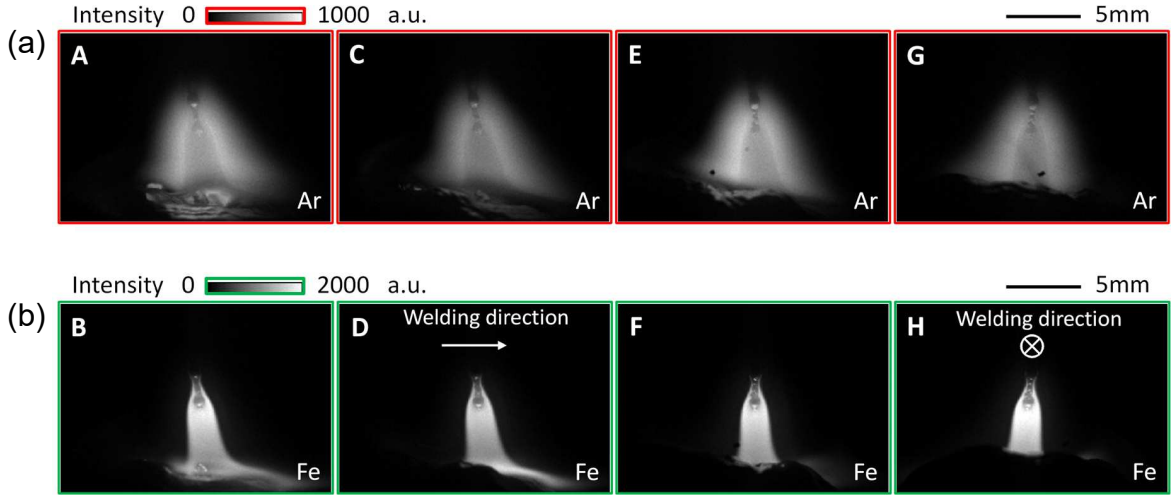

Figure 2.9: (a) argon and (b) iron dominated arc regions for spray transfer mode. Argon region imaged using Ar I spectral line (696.5 nm wavelength narrow band pass filter) and iron rich region imaged using Fe I spectral line (538.1 nm wavelength narrow band pass filter). Adapted from Namura et al. [7].

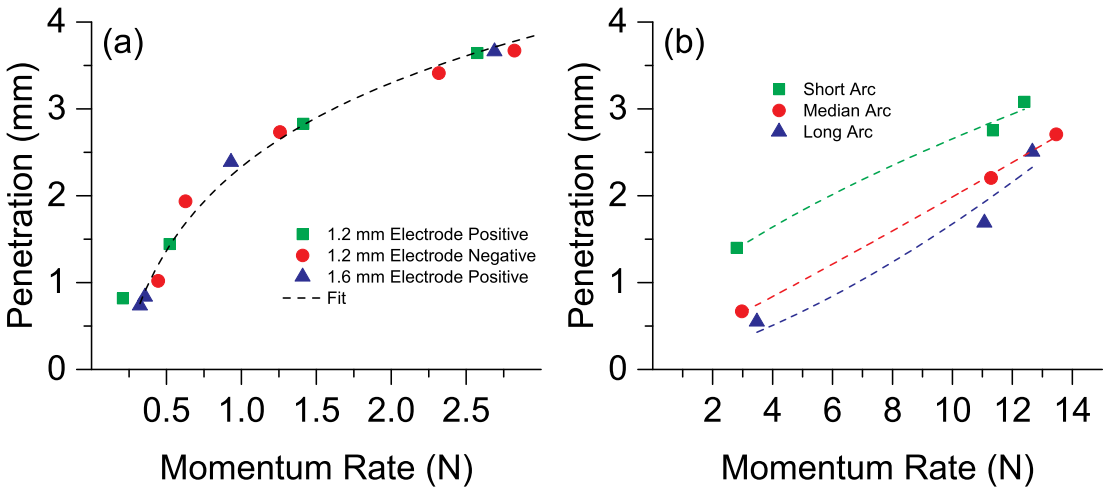

Figure 2.10: Variation penetration and momentum rate from droplet speed (a) for different wire diameters and polarity, adapted from Essers and Walter [8]; (b) for same wire diameter and electrode polarity for different arc length, adapted from Scotti and Rodrigues [9].

observed, however showing that arc length should also be considered, given that for a given momentum rate value, shorter arc length provides a deeper penetration and vice-versa.

Although there is a relationship between momentum rate and bead penetration, Scotti and Rodrigues pointed out the fact that this parameter does not take into consideration the effect of time in which the droplet is impinging on the same area of the weld pool. They took one step further and incorporated the influence of time, by introducing the term effective momentum, which is the ratio between momentum rate and welding travel speed. Welding speed should be taken into consideration given that for a given momentum rate, slower travel speeds will yield deeper weld beads compared to faster travel speeds. The variation of bead penetration and effective momentum is shown in Figure 2.11, and one can see that despite higher effective momentum conditions, there is still a strong dependence on arc length together with momentum to achieve penetration.

In a more generalized way, Murray and Scotti [10] modeled the depth of penetration in GMAW by correlating it to dimensionless magnitudes of heat and mass transfers. The mass transfer number, A, was defined as relationship between the melting rate of the electrode, $\dot{M}$, the weld pool viscosity, μ, and the radius of droplets impinging on the pool,

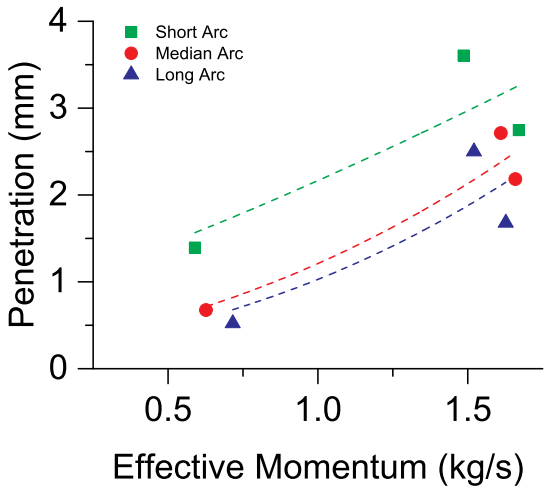

Figure 2.11: Variation of bead penetration with effective momentum. Adapted from Scotti and Rodrigues [9].

r, according to Equation 2.9.

$$A = \frac{\dot{M}}{\mu r} \tag{2.9}$$

The heat transfer number, B, was defined as a function of arc voltage, V, current, I, the change in enthalpy of the base metal that is heated from the initial temperature to the melting temperature, ΔH, welding travel speed, s, and thermal diffusivity, α, according to Equation 2.10. Using this analysis, good agreement between experimental and predicted results was achieved, and the authors concluded that heat transfer has the greatest influence on the depth of penetration, compared to mass transfer.

$$B = \frac{VIs}{\Delta H \alpha^2} \tag{2.10}$$

Despite the interplay of mass and heat transfer on weld bead penetration, these results show that bead penetration in GMAW welding can be tailored by controlling the droplet velocity, hence it is useful to have the understanding of how the process parameters alter the velocity of the impinging droplet at the moment that it hits the weld pool. For pulsed GMAW operating under the so called regime of one-droplet-per-pulse (ODPP), if

the pulse parameters are set to maximize droplet speed, bead penetration can be enhanced. This is particularly interesting when considering pulsed GMAW, which generally transfers metal in a controlled spray mode with on average current lower than that if constant voltage was used, giving lower penetration when compared to constant voltage GMAW. Research has been published reporting experimental data of droplet speed [8, 73, 9], while others have attempted to predict the droplet speed based on mathematical modelling of heat and mass transfer [74, 73, 75, 76]. Most of the experimental work reporting droplet velocity considers constant voltage GMAW [38]. A number of experimental work have been published investigating the influence of pulse profile on metal transfer [40, 77, 59, 78, 79], but few of them have specifically focused on the influence of pulse profile on droplet velocity.

Chapter 3

Experimental

3.1 Material

To investigate the influnce of pulse profile and process parameter on metal transfer, bead on plate welds were performed using AWS A5.18 ER70S-6 wire. The wire electrode had a 1.2 mm (0.045") nominal diameter. The base metal was 1020 steel plates of 9.5 mm thickness. The shielding gas used was a mixture of 85% Ar-15% CO_2 at at flow rate of 18.9 l/min (40 cfh).

For the metal transfer and arc phenomenon imaging, a high-speed camera (FASTCAM Mini UX50, Photron, USA) was used. The lens used was a C-mount close focus zoom lens (6X, 18-108 mm FL, Edmund Optics Inc., USA) equiped with a 25/25.4 mm diameter C-mount lens mounts (Thick Lens Mount from Edmund Optics Inc., USA) to incorporate bandpass filters, which were used to limit the amount of light from the arc reaching the camera sensor, allowing to reveal different features of the arc and/or molten metal, at both wire electrode and weld pool.

Bandpass interference filters of two wavelengths, 515±10 and 900±10 nm, were used. The 515±10 nm wavelength allowed the imaging of the features in the arc core, which is composed mostly of high fraction of iron vapor. The imaging of iron vapor is possible owing the fact that iron has a strong peak emission line at a 516.74 nm wavelength [80–82].

To capture the outer cone of the electric arc, droplet formation and transfer, and weld pool dynamics, a narrow band pass filter of 900 ± 10 nm wavelength was used. The lens aperture was fixed at $f/22$ and different exposure times were used.

Two pulse profiles were investigated. The first, Fig. 3.1(a), have a exponential current increase from background to peak value, and a long tail decay from peak to background current (Lincoln PowerWave R500, Lincoln Electric, USA). The second current profile, Fig. 3.1(b), has a nearly ideal square pulse shape (Liburdi Dimetrics GoldTrack VI, Liburdi Engineering Limited, Canada).

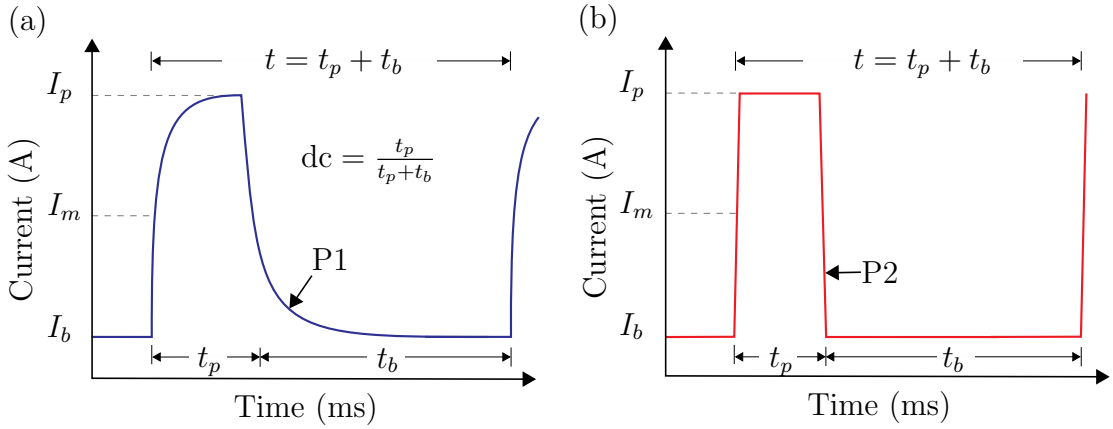

Figure 3.1: Investigated pulse profiles: (a) profile 1 (P1) with a exponential current change and (b) profile 2 (P2) nearly square.

3.2 Methodology

3.2.1 Welding Procedure

The metal transfer was investigated for a range of wire feeding speed raging from 150 to 300 ipm (inches per minute). To investigate the influence of pulse parameter on metal transfer, each current pulse profile was used in the form of two distinct settings: low and high I_b/I_p current ratios, as shown in Fig. 3.2.

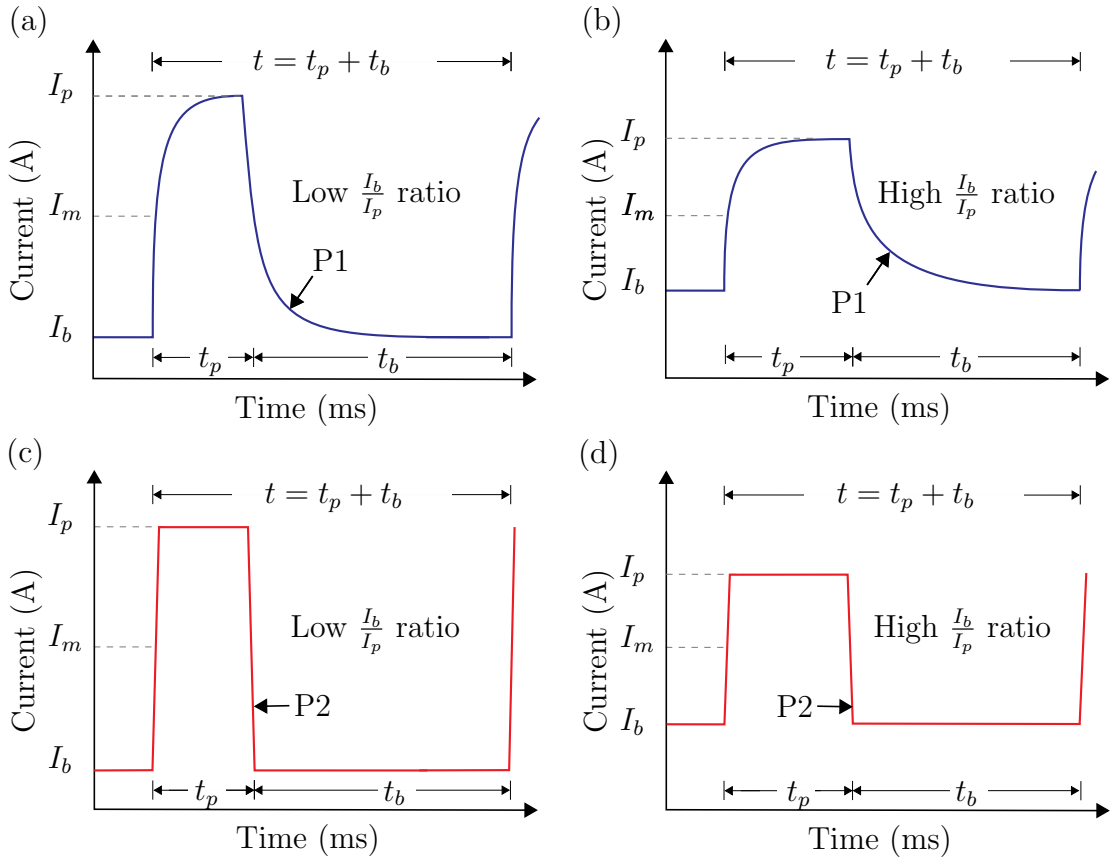

Figure 3.2: Pulse profiles settings for conventional pulse (a) low and (b) high I_b/I_p ratio, and ideal square wave pulse (c) low and (d) high I_b/I_p ratio.

The welding parameters were set to achieve metal transfer mostly in the one droplet per pulse transfer (ODPP) regime. For each wire feeding speed, at low and high I_b/I_p ratio, the welding parameter for the different profiles were set to be the equal: same peak and background current, travel speed, arc voltage and pulse frequency. In order to achieve that, the current duty cycle was adjusted automatically by the power supply. This allowed a direct comparison of the influence of pulse profile on the droplet formation and transfer mechanisms. In order to ensure reproducibility of the results, for each condition five replicates were performed for each condition.

3.2.2 Droplet formation and transfer monitoring

To monitor droplet formation and detachment, the high speed camera recording the arc at a frequency of 5000 frames per second, was synchronized with a data acquisition system (DAQ), which was recording the welding current and voltage at a frequency of 20 kHz for a period of 1 s. The bandpass filters were used to limit the amount of light reaching the sensor. Due to the nature of pulsed GMAW welding, where there are periods of excessive high and low brightness throughout the pulse period, due to the high and low current values, and so the camera was operated at different exposure times, in order to capture the events occurring during the phase of peak and background phase.

To measure droplet transfer velocity, the droplet position was tracked manually, by using the image processing software ImageJ [83], in which the coordinates (x, y) of the center of the droplet was captured manually by using the built-in software "Point tool" tool. To do so, the center was determined as being the intersection of two straight lines drawn across the droplet diameter. Figure 3.3 shows an example of an image acquired when the events occurring during background period were being observed. This figure also shows how the droplet position was tracked in order to calculated its velocity across the arc and impinge onto the molten pool.

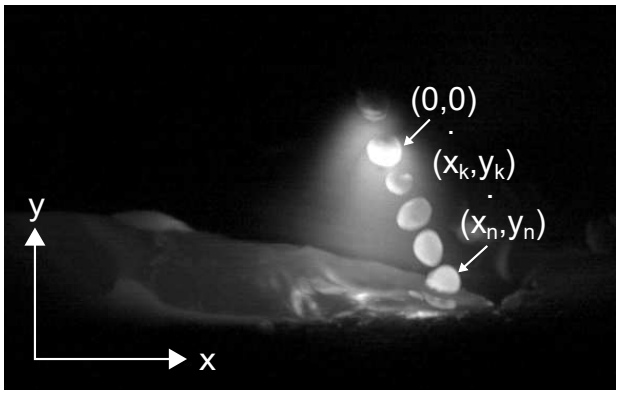

Figure 3.3: Schematic of droplet position tracking with 5 frames of the same droplet overlaid from multiple times during the transfer from wire to weld puddle..

The droplet position and time were taken as being both zero right after detachment,

then the change position of droplet center was monitored in the subsequent frames. This allowed one to determine the value of position for each time. Then, the centred numerical derivative, Equation 3.1, was employed to calculate the droplet speed as it travels across the arc, where Δt is the time between two subsequent frames, equal to 0.2 ms.

$$v = \frac{x(t + \Delta t) - x(t - \Delta t)}{2\Delta t} \tag{3.1}$$

The droplet velocity was taken as the average of the speeds calculated between detachment and impingement onto the weld pool. The reported values are the arithmetic mean of the speed of 10 droplets.

Droplet diameter was evaluated by measuring the droplet area manually using the "Freehand Selection" tool, and then an equivalent droplet diameter was calculated by approximating it to a spherical shape, $d = \sqrt{4\pi A}$, where A is the measured area in mm^2. As it can be noted from Fig. 3.3 that the measured droplet diameter is an approximation given that the droplet shape and size changes as it travels through the arc. To increase the accuracy of the measurements, droplet diameter was measured when the droplets were at a random position in the between wire tip and weld pool. This procedure was repeated for 30 droplets and the droplet diameter reported in is the arithmetic mean of these.

3.2.3 Droplet velocity prediction

Using the data of droplet speed measured, a neural network (NN) was trained to predict droplet speed. The NN training exercise was performed using the Experimenter application from Waikato Environment for Knowledge Analysis (WEKA) software (version 3.8, University of Waikato, Hamilton, New Zealand) [84]. The WEKA's software classifier used was the *MLPRegressor*, which trains a multilayer perceptron algorithm using WEKA's optimization class by minimizing the given loss function plus a quadratic penalty with the Broyden-Fletcher-Goldfarb-Shanno (BFGS) method [84]. The *MLPRegressor* has only one hidden layer, and uses sigmoid as the activation function in the hidden layer and squared error as the loss function. For this study, the NN algorithm performance was evaluated based on the Pearson's correlation coefficient. To increase the reliability of the model by

reducing the prediction error, and prevent over-fitting of the predictive model, the NN was trained using non-exhaustive k-folds cross-validation technique [85, 86].

Chapter 4

Welding Parameters and High-speed imaging

Overview

This chapter is divided into two main sections. In the first section, the welding paramters required to achieve metal transfer in the one-droplet-per-pulse (ODPP) regime are presented and discussed. In the second section, the high-speed camera images are shown for different camera settings and selection of filters.

4.1 Welding parameters

Table 4.1 gives the input welding parameters for the range of welding speed investigated for both profiles. These parameters provided metal transfer mostly in the one-droplet-per-pulse (ODPP) regime. Note that for a given wire feeding speed both profiles have the same input process parameters, for pulse settings of low and high I_b/I_p ratio. Additionally, for each wire feeding speed, the average voltage was the same for both profiles for both low and high current ratio. In order to achieve that, the pulse duty cycle had to be changed. This was intentionally conditioned so the comparison of metal transfer could be made

while using the same currents and wire feeding speeds. From Table 4.1 one can note that the pulse frequency is lower for both profiles when high peak and low background current values are used.

Table 4.2 shows give the output process parameters. As shown on this table, when the same process parameters are used to deposit metal at same wire feeding for the different profiles, the duty cycle is shorter for profile 2 (P2), and for the setting of higher peak and lower background current. For the same set of welding parameters, profile 2 requires the shortest duty cycle for metal transfer. As a consequence of that, profile 2 uses the lowest average current and instantaneous average power, and consequently lowest heat input, for metal transfer, for all the wire feeding speeds evaluated in this study as noted. This can be seen on Table 4.2. If one compares the instantaneous average power for a given wire feeding speed, the difference in the instantaneous average arc power is of around 1000 W between profile 1, at high current ratio, and profile 2 at low current ratio settings.

For the purpose of comparison, an attempt was made to use equal voltage for the different pulses at the same wire feeding speed. However, when low current ratios was used, the average arc voltage and travel speed have to be lower to maintain a smooth bead surface appearance by avoiding the formation of ripples owing to the lower pulse frequency and lower background current. Although peak current uses a high value, it will stay at the peak for a limited time, given the low duty cycle, and the low value of backgroung current does not provide enough arc presure to smooth out the solidifying weld pool and avoid the formation of the welding ripples [76, 87]. The lower travel speeds is used to make sure that the arc stays over the weld pool for a longer time.

Considering this need to decrease the travel speed, the nominal heat input is not necessarily proportional to the average current and instantaneous average power. Figure 4.1 shows the variation of average current and nominal heat input for all the profiles and wire feeding speed. On Figure 4.1(a) one can see that for all wire feeding speeds, profile 2 with high peak and low background current, low I_b/I_p ratio, uses the lowest average current and profile 1 at high I_b/I_p ratio, lower peak and higher background current, and requires the highest average current. Accordingly, profile 2 at low I_b/I_p current ratio setting, have the lowest heat input value. On the other hand, profile 1 using the low I_b/I_p current ratio setting produces the highest heat input values, and not profile 1 at high I_b/I_p current ratio

Table 4.1: Input welding parameters for one-droplet-per-pulse metal transfer regime.

Wire feeding speed (ipm[a])	Current ratio	Profile	Welding Speed (ipm)	Pulse frequency (Hz)	I_p (A)	I_b (A)
150	High	P1	12	140	375	50
		P2				
	Low	P1	10	110	510	30
		P2				
200	High	P1	10	170	380	75
		P2				
	Low	P1	10	150	520	40
		P2				
250	High	P1	14	220	400	100
		P2				
	Low	P1	12	180	520	45
		P2				
300	High	P1	14	240	400	115
		P2				
	Low	P1	12	220	530	55
		P2				

[a] ipm = inches per minute.

setting, which have the highest average current and instantaneous average power. It can therefore be concluded that for GMAW-P, square current profile, profile 2, allows the transfer in the ODPP regime with the lowest heat input, when compared to the exponential profile.

Table 4.2: Output welding parameters for one-droplet-per-pulse metal transfer regime.

Wire feeding speed (ipm[a])	Current Ratio	Profile	I_m (A)	Voltage (V)	Power (W)	dc (%)	t_p (ms)	Heat input (kJ/mm)
150	High	P1	138	21.5	3308	27.0	1.93	0.651
		P2	115	21.5	2840	19.9	1.42	0.559
	Low	P1	110	20.2	2842	16.6	1.51	0.671
		P2	90	20.0	2323	12.4	1.13	0.552
200	High	P1	167	22.6	4110	30.3	1.78	0.809
		P2	152	22.5	3788	25.4	1.49	0.746
	Low	P1	155	22.1	4143	23.9	1.54	0.815
		P2	123	22.0	3396	17.4	1.16	0.669
250	High	P1	218	24.1	5514	39.3	1.82	0.930
		P2	183	24.9	4860	27.7	1.26	0.820
	Low	P1	176	23.3	4874	27.5	1.55	0.959
		P2	147	23.3	4210	21.6	1.20	0.833
300	High	P1	237	25.6	6363	43.0	1.79	1.074
		P2	212	26.2	5924	34.1	1.42	1.000
	Low	P1	224	24.9	6344	35.6	1.62	1.249
		P2	177	24.4	5180	25.8	1.17	1.021

[a] ipm = inches per minute.

4.2 High-speed imaging[1]

In this section the results of the high-speed imaging are presented. Different camera settings were used in order to reveal different features of the arc phenomena and metal transfer. For evaluation of the camera settings, only profile 2 was used. For this set of experiments the welding conditions were wire feeding speed of 150 ipm; travel speed of 7.5 ipm; peak current $I_p = 400$ A; background current $I_p = 50$ A; pulse frequency of 90 Hz, and voltage

[1] The contents of this section of the chapter have been incorporated within a paper that has been submitted for publication. E. B. F. Dos Santos, L. H. Kuroiwa, A. F. C. Ferreira, R. Pistor and A. P. Gerlich, "On the visualization of gas metal arc welding plasma and the relationship between arc length and voltage". Submitted to the journal *Applied Sciences*. Submission date March 18, 2017.

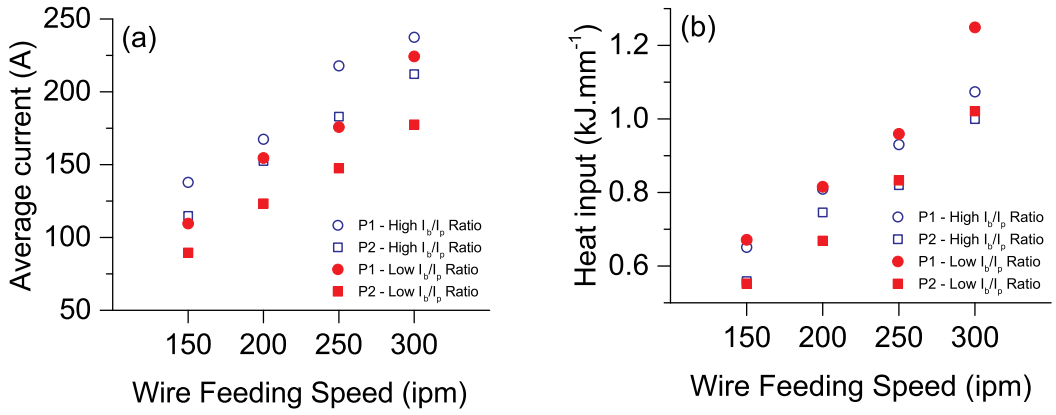

Figure 4.1: (a) variation of average current and (b) nominal heat input with wire feeding speed.

of 20 V.

Figure 4.2 shows the images acquired when the arc radiation was filtered with a 515±10 nm narrow band pass filter for different camera sensor exposure times. In this figure, the camera exposure time is varied from 3.91 to 80 μs. Each column of this figure shows the images from the start of peak phase to the onset of background current. Iron (Fe) has a strong emission peak (Fe I) at the wavelength of 516.74 nm [80], and hence using a narrow band pass filter of 515±10 nm wavelength will limit the passage of radiation that is mostly from Fe I. Hence, the bright regions on these images are composed mostly of iron vapour, given that the only light passing through the filter is in the range of this characteristic iron emission peak. Although iron has a peak emission line at 515±10 nm wavelength, other radiation is also able to reach the camera sensor. As a consequence of that, increasing exposure time will allow more radiation to reach the camera sensor, over-exposing the image, leading to image flare. This can be seen on the fifth row of Figure 4.2 for the exposure times of 20, 40 and 80 μs.

Despite the image flare due to the excessive sensor exposure, 3.91 and 6.25 μs exposure times allow to the imaging of the iron vapor formation and evolution during the current pulse period. In Figure 4.2 at the times of 123.0 and 79.8 ms for the exposure time of 3.91 and 6.25 μs, respectively, that the light captured by the camera sensor is being emitted

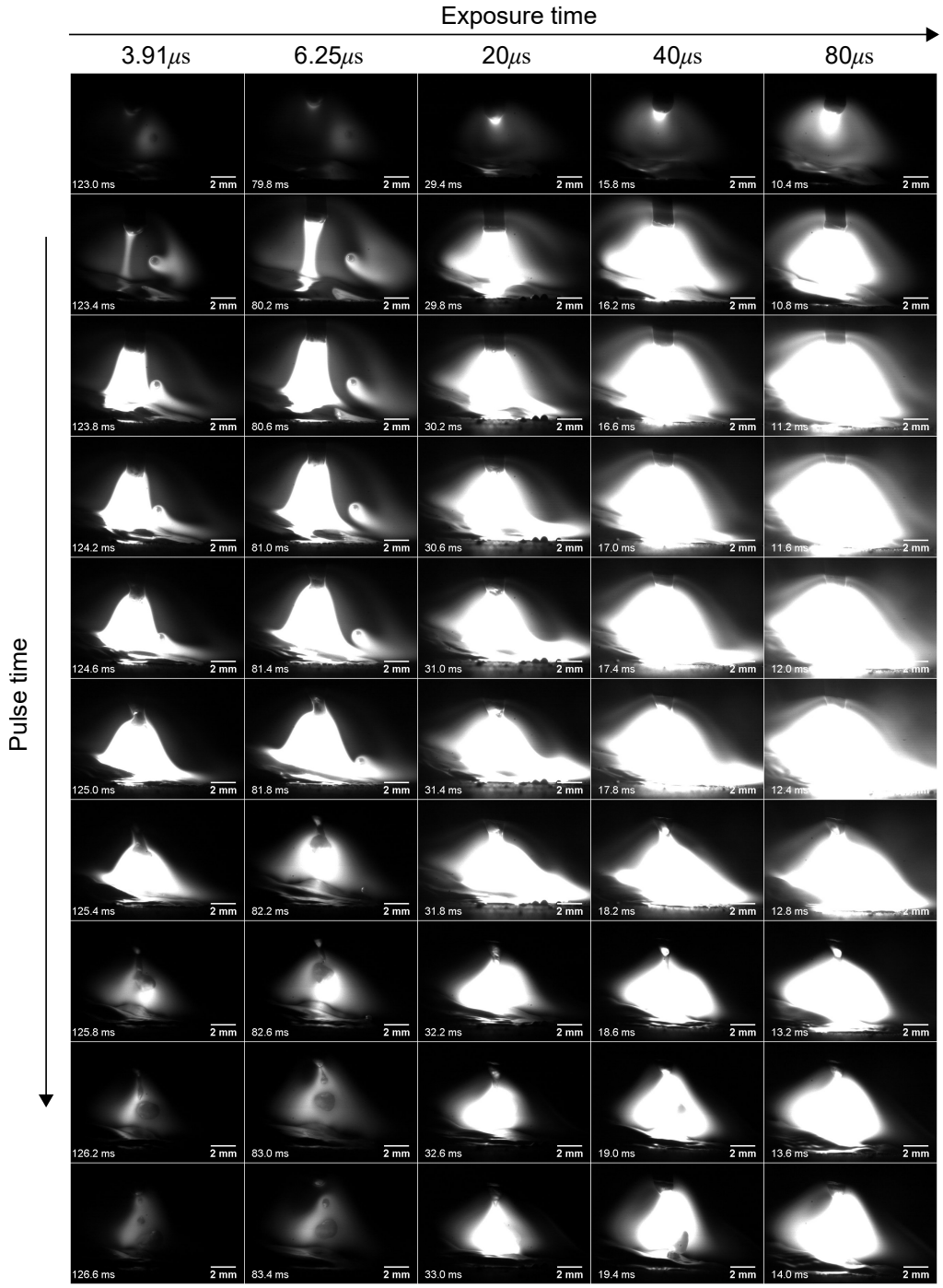

Figure 4.2: Arc appearance for aperture of f/22 using at narrow band pass filter of 515±10 nm wavelength for different camera sensor exposure time.

from the wire tip, weld pool and the small droplet being transfered. Those regions are the main source of iron vapour owing to the high temperature of their surfaces [71, 66]. As the current increases to peak phase, the amount of vapour emitted from the wire tip increases due to the increase in wire tip temperature. This evolution of metal vapour region has been repeatedly predicted by numerical simulations [66, 44, 69]. Additionally, on Figure 4.2 for the exposure time of 3.91 and 6.25 μs, one can see that the metal vapour around the secondary droplet is pushed downward away from the molten pool, as the pulse current increases to peak value, owing to the increase in plasma flow velocity as a consequence of the current increase [61]. Boselli et al. [68] has numerically shown that this metal vapour pushed to lower temperature arc regions will lead to fume formation.

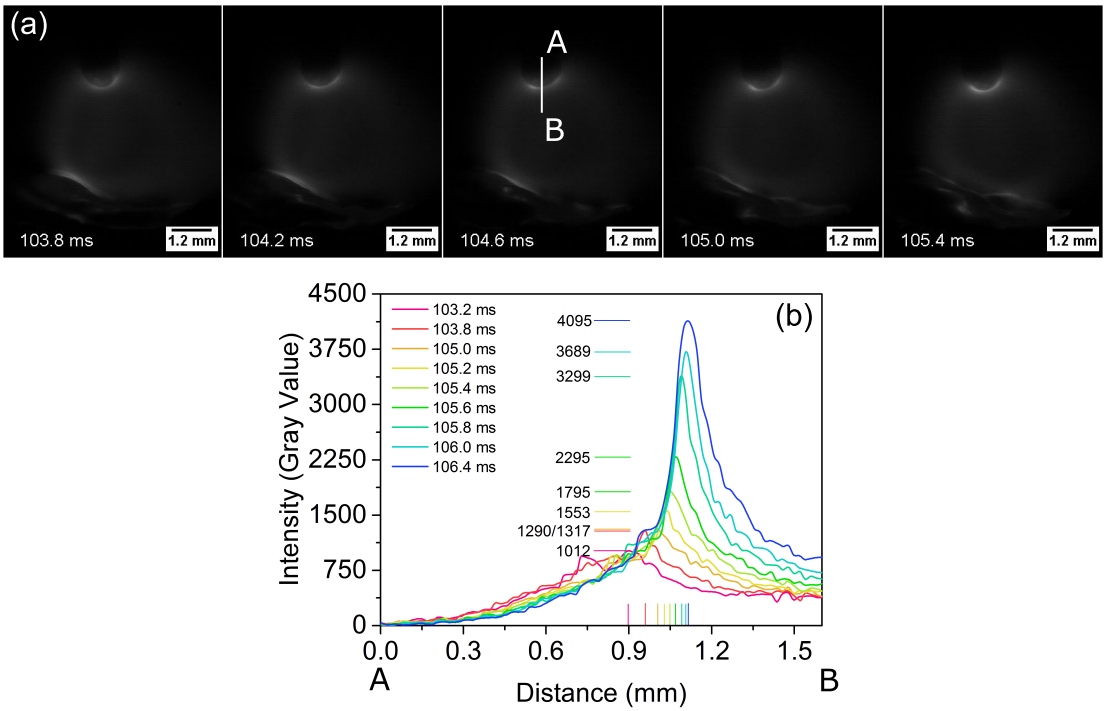

Figure 4.3: Pixel intensity at wire tip for a current of 55 A, observed with an aperture of f/22 using at narrow band pass filter of 515±10nm wavelength and exposure time of 80 μs.

Given that when the 515±10 nm wavelength filter is used, the image brightness is proportional to the amount of high temperature iron vapour, one could use this information

and correlate the image pixel intensity to the amount of iron vapor present in a specific region. This is shown on Figure 4.3, where images were taken during current background phase with an exposure time of 80 μs. The evolution of brightness for pixels along line A in Figure 4.3(a) are ploted in Figure 4.3(b). It can be seen that the pixel intensity (gray value) increases with time, indicating an increase in the amount of iron metal vapour in the wire tip. This is in agreement with numerical simulation of Boselli et al. [66] where was shown that during background current phase iron vapour accumulates at the wire tip and it not dragged down by the plasma flow due to the slow flow velocities owing to the small current values.

In Figure 4.4 the evolution of arc and droplet formation during the current pulse (for the same welding conditions corresponding to Figure 4.2) are shown for different exposure times when a 900$\pm$10 nm wavelength narrow band pass filter is used. In this figure, the camera exposure time is varied from 6.25 to 160 μs. Compared to those acquired with the 516$\pm$10 nm filter, these images provide more details of the droplet formation sequence and weld pool motion. An exposure time of 20 μs allows simultaneous visualization of the arc, droplet formation and molten pool motion. Indeed, at an exposure time of 20 μs, one can distinguish an inner brighter cone in the arc, which can be compared to the 515$\pm$10 nm wavelength filter to reveal that this brighter inner cone is the iron vapour core of the arc. This is shown in Figure 4.5 where the snapshots at equivalent times taken using both filter are compared. Therefore, the 900$\pm$10 nm wavelength filter allows to visualize both regions of the arc, i.e. the inner cone with a high fraction of iron vapour and the outer cone composed of mostly ionized shielding gas, which is Ar in the present investigation.

For all the filters and camera settings tested in this work, it was found that when the 900$\pm$10 nm wavelength filter is used with camera exposure time of 80 and 160 μs, it provides clear pictures of the events occurring during background phase of current pulse profiles allowing monitoring of droplet transfer and weld pool motion. This is shown on Figure 4.6.

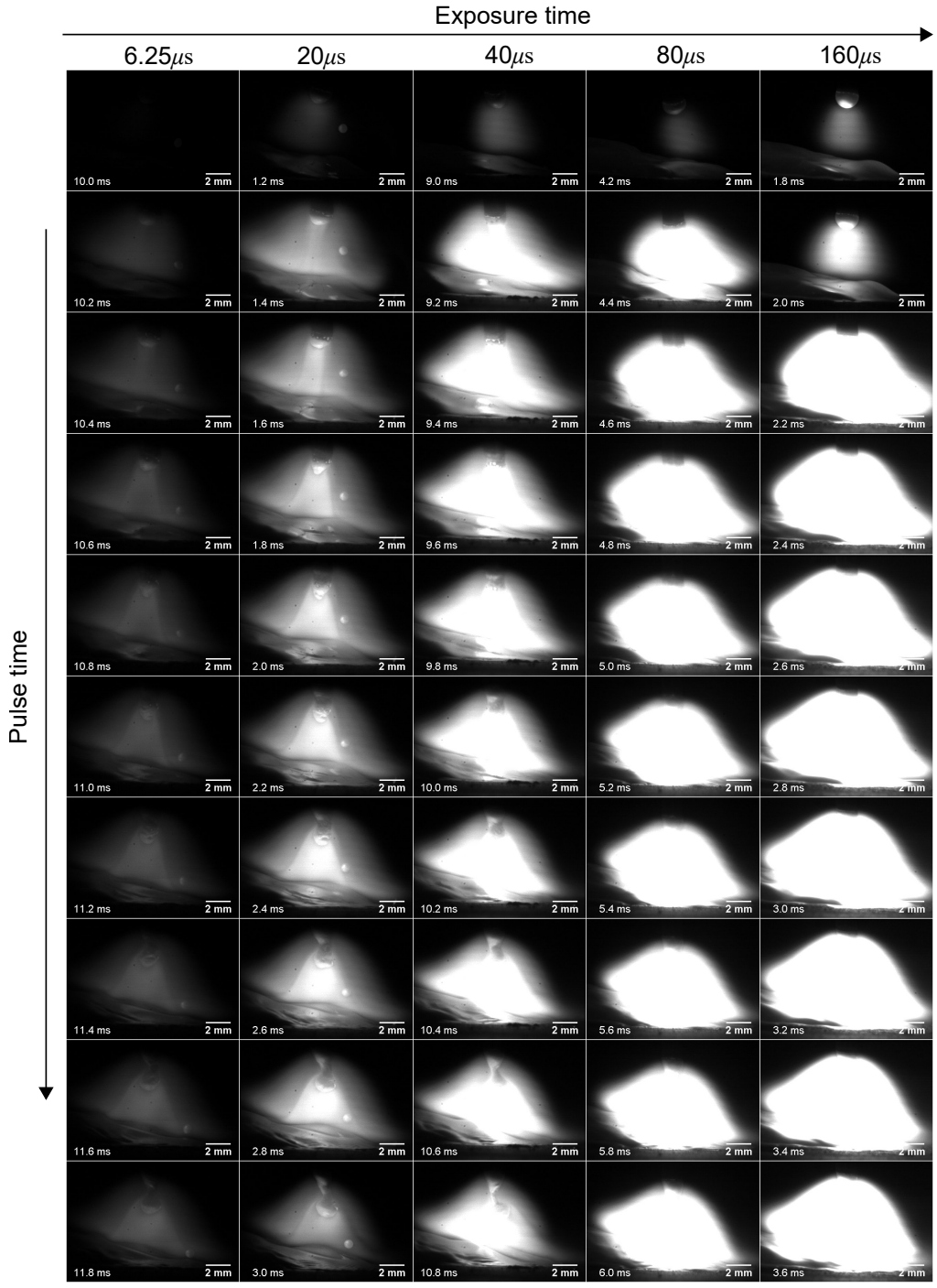

Figure 4.4: Arc appearance for aperture of f/22 using at narrow band pass filter of 900±10 nm wavelength for different camera sensor exposure time.

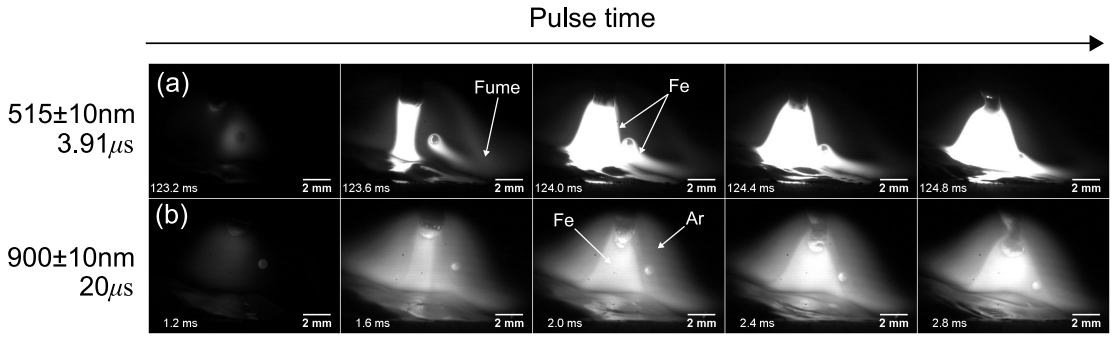

Figure 4.5: Iron (Fe) metal vapour and argon (Ar) dominated regions (current of 400 A).

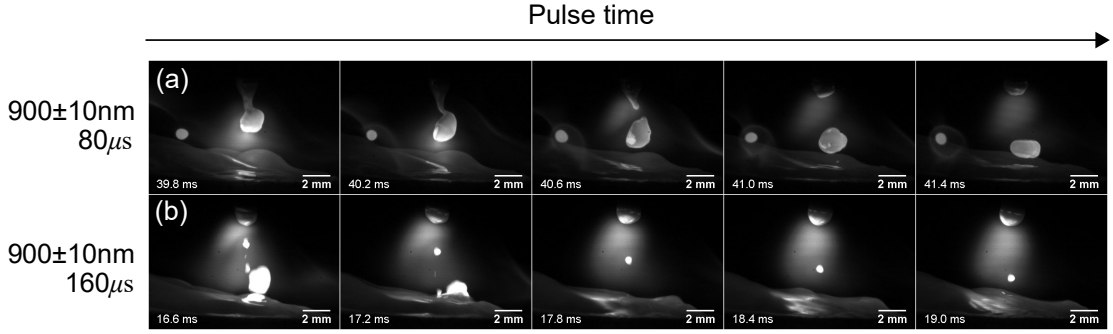

Figure 4.6: Setting that can be used for (a) droplet temperature measurement and (b) weld pool behavior (current 50 A).

Chapter 5

Metal transfer and bead characteristics

Overview

This chapter is divided into two main sections, the first, Section 5.1, presents the comparative analysis of metal transfer for the two current pulse profiles investigated for a range of process parameters. The metal transfer for both profiles is compared in terms of droplet formation, detachment and finally the velocity of the detaching droplet is evaluated. In the second section of this chapter, Section 5.2, the correlation between metal transfer and bead geometric and metallurgical characteristics are discussed.

5.1 Metal transfer[1]

5.1.1 Droplet formation

Figures 5.1 through 5.4 show the sequence of events occurring during droplet formation and detachment for the two profiles and settings investigated. It was found that the longer time taken by profile 1 to reach background current has a consequence on the amount of necking that the molten metal at the wire tip undergoes before base current is reached. This is shown on Figure 5.1, where the droplet formation was observed during peak time. It was verified that at the end of peak phase the necking diameter was 0.46 mm for profile 1, while for the same conditions the diameter was 0.74 mm when profile 2 is used. In Figures 5.3 and 5.4 the arc was recorded during the base current phase and this difference between the profiles is even more clear, regardless of the current ratio used. Compare the necking diameter at the moment that background current is reached, at 2.4 ms in Figure 5.4(a) versus 3.2 ms in Figure 5.4(b). This observation was consistent throughout the range of parameters investigated and more evident for the conditions where low I_b/I_p ratios were used. The stronger necking observed in Fig. 5.1 when the pulse assumes background current, for profile 1, is caused by the strong electromagnetic pinch acting on the liquid metal column for a longer time, due to the slow decay in current for this profile, compared to the reduced time in profile 2 due to the sharp drop in current from peak to background.

The ratio between background and peak current, I_b/I_p, also has an influence in droplet formation. It was found that if low I_b/I_p ratios are used, i.e. higher values of peak currents, most of wire melting and droplet formation occurs during peak phase of current, as well as an longer necking is observed. This can be observed by comparing Figure 5.3 to 5.4. It is possible to see that using a high I_b/I_p ratio, Fig.5.3, the droplet is still being formed when the pulse assumes background current, while for the condition where this ratio is low,

[1]The content of this section of the chapter have been incorporated within an Accepted Manuscript of an article published by Taylor & Francis in *Science and Technology of Welding and Joining* on February 21, 2017, available online: http://wwww.tandfonline.com/10.1080/13621718.2017.1288889. E. B. F. Dos Santos, R. Pistor and A. P. Gerlich, "Pulse profile and metal transfer in pulsed gas metal arc welding: droplet formation, detachment and velocity".

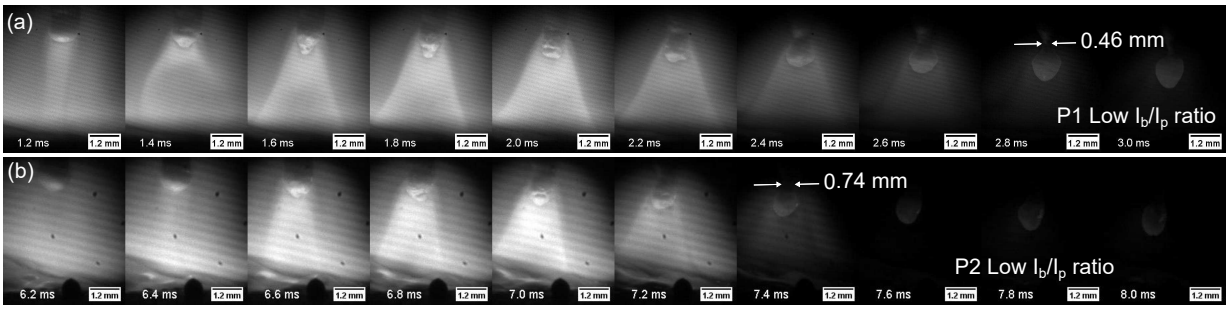

Figure 5.1: Droplet formation for profiles 1 and 2 at a wire feeding speed of 200 ipm recorded during peak current phase.

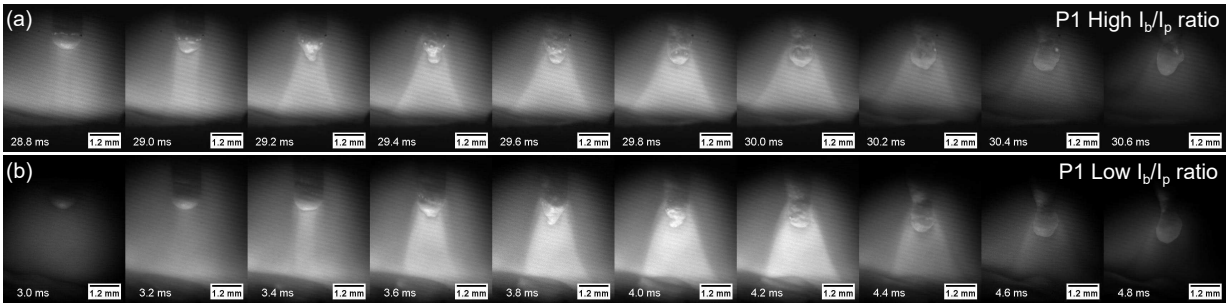

Figure 5.2: Droplet formation for profile 1 at a wire feeding speed of 150 ipm for the (a) high and (b) low I_b/I_p current ratios.

Figure 5.4, it is clear the droplet already formed. Whether or not the droplet is already formed at the moment that background current is reached will have a direct effect on the droplet speed as will be explained later.

Figure 5.1 suggests the brighter inner cone composed of iron vapour content, formed due to evaporation of the overheated electrode tip [71, 5, 63, 66]. It is noticeable that metal vapour is generated for a shorter time when profile 2 is used, compared to profile 1. Additionally, this high iron vapour region is narrower for profile 2. Narrower iron vapour plasma streams also observed when comparing setting of high and low peak currents, Figure 5.2, and it shown that a higher peak current results in a narrower arc core, which is as consequence of the stronger arc pressure, which increases with increasing peak current according to Equation 2.6.

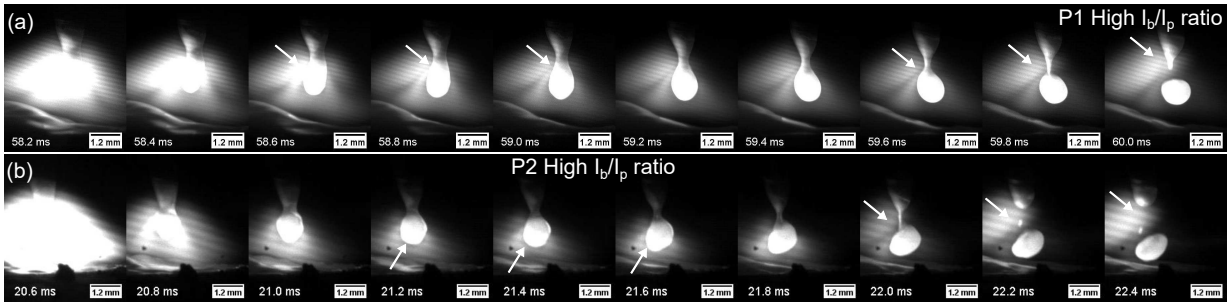

Figure 5.3: Droplet detachment for profiles 1 and 2 at a wire feeding speed of 200 ipm, when high values of I_b/I_p current ratio is used. The arrows indicate the arc attachment position for each time.

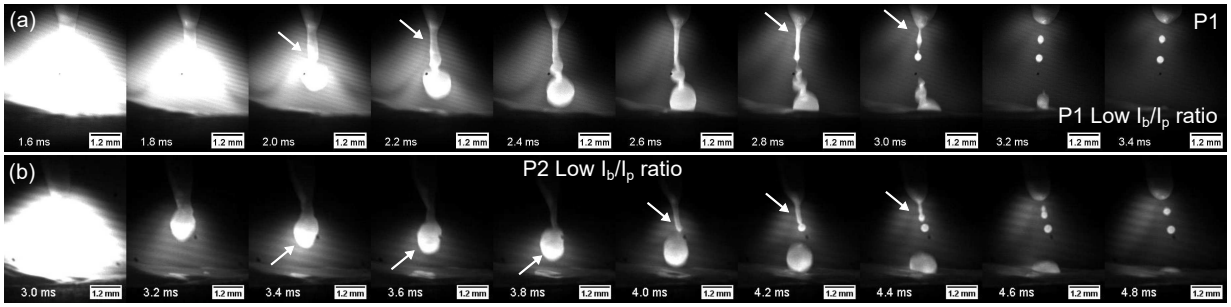

Figure 5.4: Droplet detachment for profiles 1 and 2 at a wire feeding speed of 300 ipm, when low values I_b/I_p current ratio are used. The arrows indicate the arc attachment position for each time.

5.1.2 Droplet detachment

Droplet detachment differs for both profiles, regardless of the current ratio I_b/I_p value used. Droplet detachment for profile 1 occurs at current values in the transition from peak to background, while for profile 2 the droplet detachment occurs during background current phase, and this can be seen comparing top and bottom of Figure 5.4. In Figures 5.3 and 5.4 it is possible to notice a change in the position where the arc attaches to the wire during background current when comparing both profiles. The zone of arc attachment to the wire is the region of maximum brightness in each frame in the sequence of snapshots and is indicated by the arrows.

For profile 1, the arc attaches to the wire in an area slightly above the forming droplet, on the constricted portion of the wire. On the other hand, for profile 2, the arc attachment point follows the bottom of the detaching droplet and jumps back to the wire tip only after droplet detaches. This difference between the profiles was verified for both high and low I_b/I_p current ratio settings, see Figures 5.3 and 5.4. This jump in arc attachment to the wire was also identified by monitoring the signal of voltage, and presented itself to happen consistently, see Figure 5.5. While profile 1 presents a smooth decay in voltage signal after maximum voltage is achieved, Figure 5.5(a), profile 2 shows a secondary peak in the current signal and this happens after droplet detachment at a time of 5.25 ms. This is better seen in Figure 5.6 when the images from the high speed camera are synchronised with the current and voltage signals.

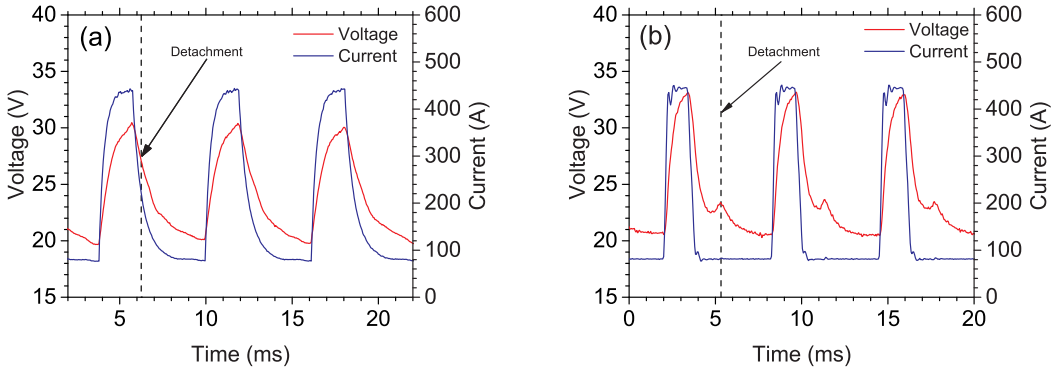

Figure 5.5: Current and voltage signal for (a) profile 1 and profile 2. The time when detachment occurs is indicated by the vertical dash line.

The observed difference in arc attachment position for the investigated profiles, can be a consequence of changes in arc plasma electrical properties due to the different amount of iron metal vapour formed. This is shown in Figure 5.1, and if one compares the top and bottom portions of this figure, it can be noted that the generation of metal vapour takes place during a longer time for profile 1, as consequence of the slow decay from peak to background current. It follows that a higher amount of current is allowed to flow through the droplet bottom for profile 2, due to the lower amount of iron vapour, while for profile 1 the high amount of metal vapour forces the arc to climb the wire to a position above the forming droplet, i.e. to the wire constriction area. This mechanism was described by

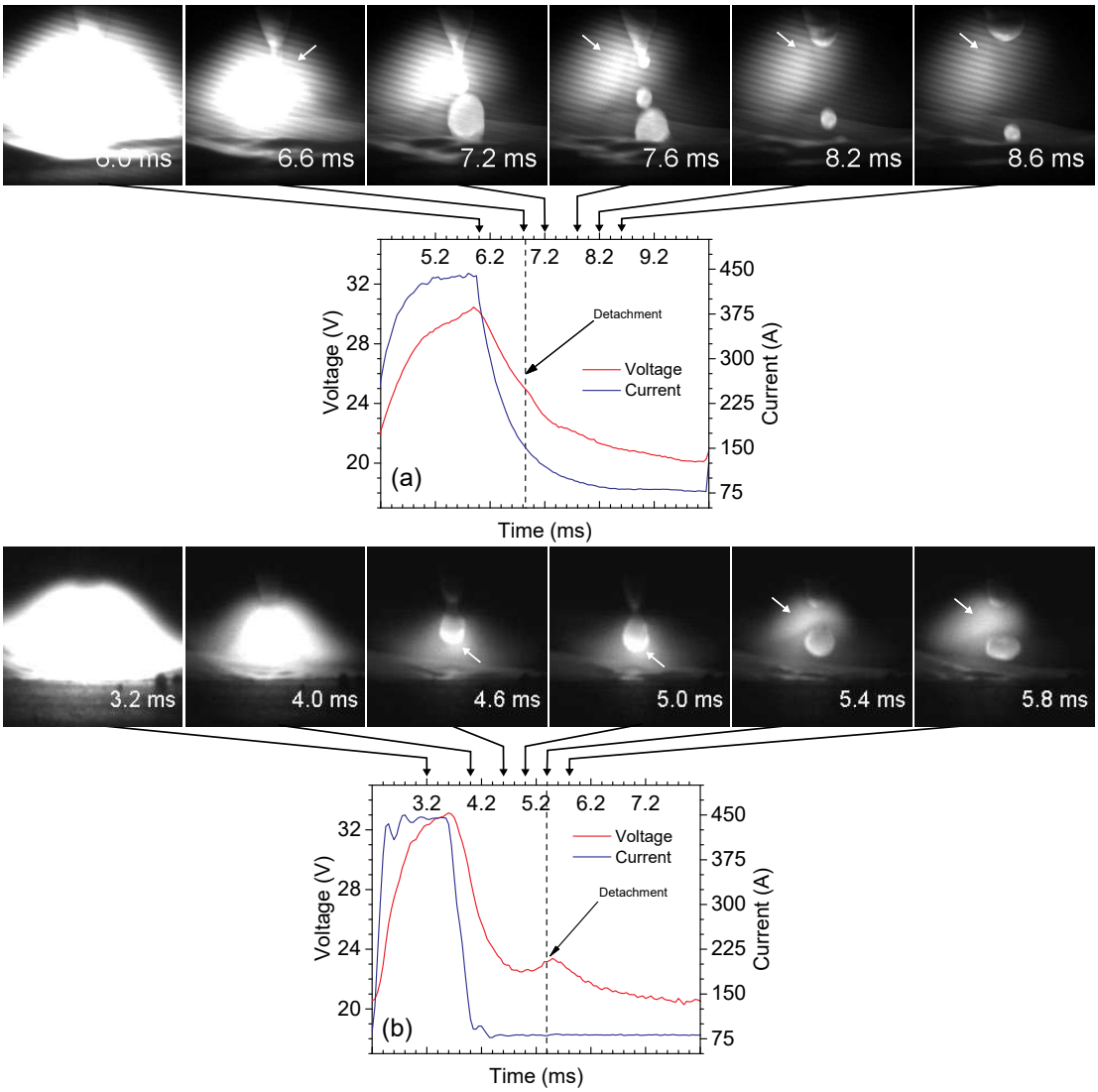

Figure 5.6: Synchronised current and voltage signals with snapshots from high speed photography. In (a) the sequence of events for profile 1 and (b) for profile 2. The arrows indicate the arc attachment position for each time.

Hertel et al. [44, 69] based on their simulation results, but has not yet been confirmed experimentally.

Although direct estimation of iron metal vapour, arc properties and current distribu-

tion were not performed, either experimentally or by numerical simulations, one major implication of the present work is to indicate that when profile 2 is used, potentially less metal vapour is generated and this helps to maintain the arc attached to the droplet bottom. Meanwhile, for profile 1 the formation of metal vapour is enhanced because it is happening for a longer time, due to the slower decrease in pulse current. This will shift the arc to attach to the wire in its constriction region, and consequently no jump in the arc attachment position is observed either in the high speed videos and on the voltage signal recordings. The possible mechanism for that, is that the larger amount of metal vapour in profile 1, which decreases the electrical conductivity at the bottom of the droplet, while on the other hand, a faster drop-off of current for profile 2 and shorter duty cycles leads to lower amounts of iron metal vapour generated, and this allows a higher amount of current to flow through the tip of the forming droplet, maintaining the arc attachment position at the tip of the wire until the droplet detaches.

5.1.3 Droplet velocity

Figure 5.7 gives the measured droplet diameter and velocity for both profiles at the different welding conditions used. Droplet diameter values vary between 1.0 to 1.2 mm, regardless of pulse profile and welding condition used. On the other hand, droplet velocity changed as the wire feeding speed and pulse settings were modified. For both profiles, the trend is that faster droplet speeds are achieved using conditions with high peak and low background currents. On this figure it is also shown that the droplet velocity tends to increase as the wire feeding speed is increased, for both profiles at low and high I_b/I_p current ratios. Note that for low values of I_b/I_p current ratio, the droplet speed is lower for profile 2, specially as the wire feeding speed increases. The increase in droplet velocity as peak current increases, shown in Figure 5.7, is a consequence of the simultaneous increase of the electromagnetic force, momentum flux and drag force, which further accelerates the droplet. As shown in Equation 2.1, the magnitude of the electromagnetic force increases with the square of current, and hence the observed increase in the droplet velocity, when low I_b/I_p current ratios are used. In addition, the force due to conservation of the momentum [3, 45] of the high speed fluid flow [88, 89, 31, 90, 44] induced within the droplet by the

electromagnetic force, Equation 2.2, also contributes to the increase in droplet speed. Lastly, once detachment occurs, the high flow developed in the plasma, which increases with the square of current according to Eq. 2.5, increases the drag coefficient which further increase the acceleration of the droplet due to the flow of the arc plasma.

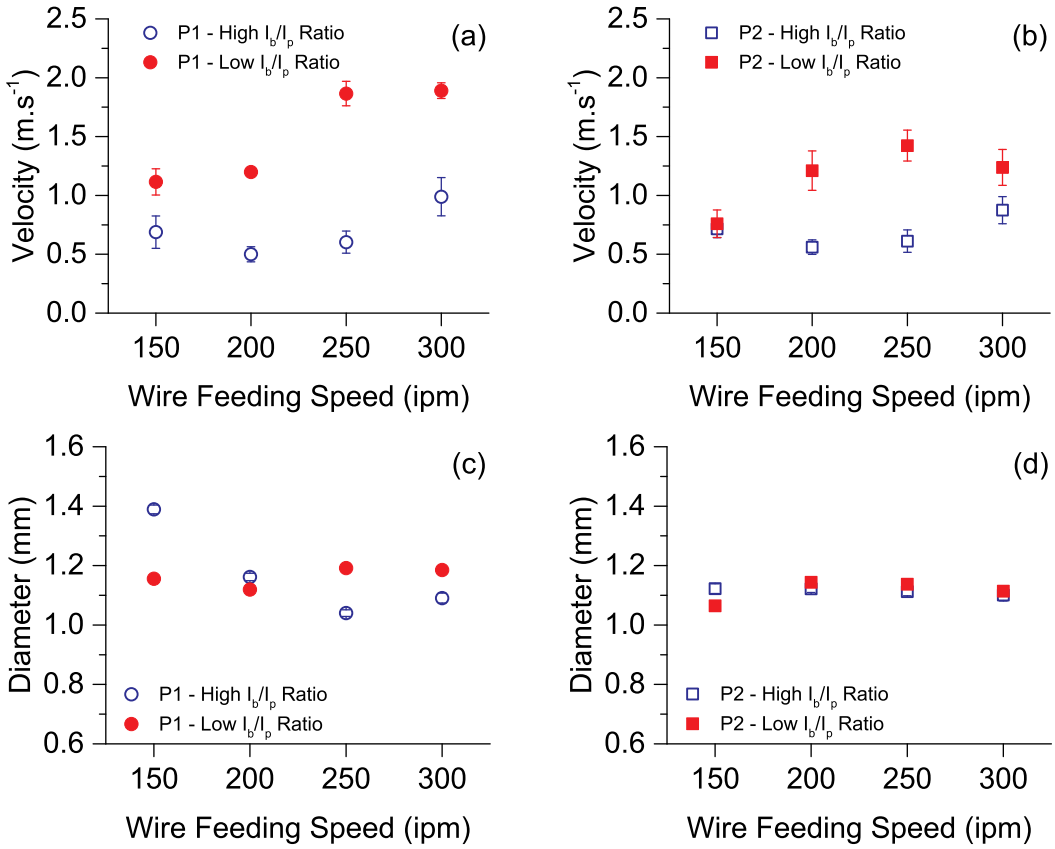

Figure 5.7: Measured droplet velocity (a-b); and diameter (c-d) for both profiles.

The increase in droplet velocity as the wire feeding speed is increased, Figure 5.7, is the same for both profiles when the high I_b/I_p current rations are used, even though droplet detachment for profile 2 occurs at a much lower current value when compared to that of profile 1. The equivalent droplet velocity of profile 2 is due to the instantaneous change in arc attachment position that follows droplet detachment, causing a sudden increase in arc pressure at the electrode tip [32, 91], which in turns accelerates the droplet. This is

seen in Figure 5.3, where comparing the droplet shape after detachment, that of profile 2 is mode elliptical, as a consequence of the high pressure at wire tip pushing the droplet, while that of profile 1 is more spherical in shape. Consequently, if the distance between the wire tip and the droplet at the moment of detachment is increased, then this effect of sudden increase in arc pressure at wire tip on droplet increasing droplet acceleration will not be as strong, and this is observed when low I_b/I_p current ratio is used. At a wire feeding speed of 300 ipm, profile 2 presents a decrease in the average droplet speed, Figure 5.7(b), compared to that of profile 1 for the same settings, Figure 5.7(a).

Another fact contributing to the decrease in droplet velocity of profile 2, when low I_b/I_p current ratio is used, is the increase in the retaining force due to surface tension. The retaining force due to surface tension is increased because of large diameter of the necking region, given that larger diameters increases the surface tension retaining force according to Equation 2.4. This difference in necking diameter is observed in Figure 5.4(b) where one can see that the droplet is still forming for profile 2 at the moment that the pulse assumes background current value, compared to profile 1 at the moment base current phase where the droplet is clearly formed. This reduced necking of the molten electrode tip of profiles 2, provides the possibility of achieving metal transfer in streaming mode, as discussed in Chapter 6 of this thesis.

It was also found that the increase in droplet speed with low I_b/I_p current ratios is not only due to the increase in peak current, but also due to the reduction of background current. A set of experiments where only peak and background current were separately changed, was performed using profiles 2, with the welding parameters shown on Table 5.1. The results of droplet velocity are shown on Fig. 5.8. Indeed, droplet speed is increased as the peak current increases, but also note the increase in droplet velocity as the background current is reduced. A variation of 100 A in peak current promoted a increase of only $0.37\,\mathrm{m.s^{-1}}$ in the droplet speed, on the other hand, an increase of $0.54\,\mathrm{m.s^{-1}}$ is observed when the background current is changed by only 40 A. Although peak and background current effect are interrelated, this result suggests that background current has a significant influence in controlling the final speed of the impinging droplet and should not be disregarded. The increase in droplet speed, with decreasing background current is due to the decrease of the retaining force due to arc pressure, Equation 2.3, which decreases with

the square of current. Lastly, one can note from Table 5.1 and Figure 5.8 that for pulsed GMAW the droplet speed is not proportional to the average current, as it is the case for constant voltage GMAW.

Table 5.1: Welding parameter of experiments performed to investigate the effect of peak and background current on droplet velocity for profile 2 (P2). Travel speed and pulse frequency were kept unchanged.

Peak Current (A)	Background Current (A)	Average Current (A)	Duty Cycle (%)	Average Voltage (V)	Average Power (W)
400	25	93.8	18.3	21.4	2610
400	45	110.2	18.4	24.9	3330
400	65	126.9	18.5	29.2	4170
350	50	153.9	18.7	22.4	2760
400	50	172.8	18.5	26.9	3550
450	50	187.2	17.4	30.1	4145

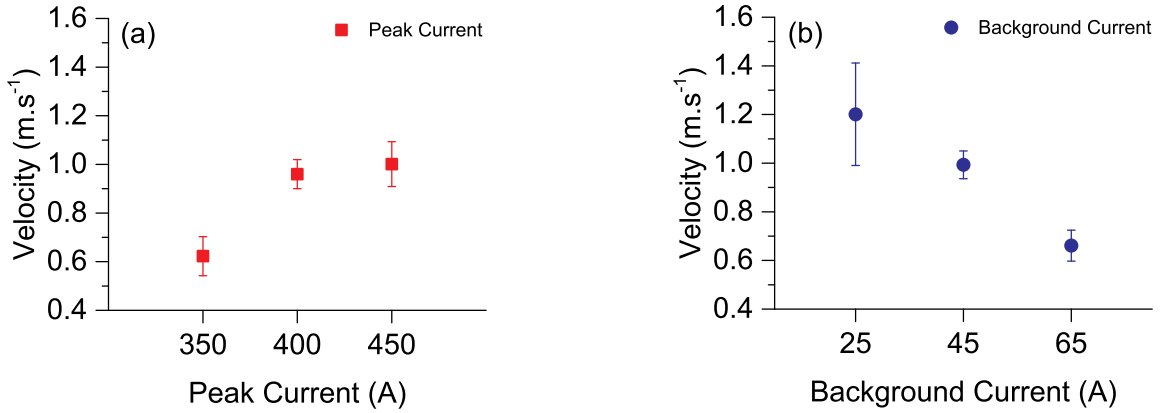

Figure 5.8: Effect of (a) peak and (b) background current on the average droplet velocity (profile 2).

5.1.4 Droplet velocity prediction

To predict droplet velocity, one could try to perform regressive analysis using the welding parameters. However, due to the intrinsic characteristics of pulsed GMAW of the interdependence of the various welding parameters, changes in welding parameters, as for example I_b and/or I_p will require changes in other parameters such as pulse frequency, f, and time at peak current, t_p. Changes in these parameters will inevitably cause variations in physical properties of both the electrode and arc plasma, such as electrode surface tension, due to change in electrode tip temperature, and plasma conductivity. That would lead to further difficulties when building a regressive model to predict droplet velocity, and a large amount of experimental data would be necessary to build a regressive model of high predictive capability. If one tries to build a regressive model, including both process parameters and physical properties, arranging all the variables in a way that the calculated number has the physical meaning of velocity, i.e. the dimension of length over time ($\mathrm{m.s^{-1}}$), this would be a cumbersome task.

One way to overcome this situation would be to predict the variation of the dimensionless droplet velocity, as a function of the dimensionless welding parameters and physical constants, and then convert this into the dimension of length over time using the appropriate methodology. This can be done based on the theory of dimensional analysis, which states that if a physical phenomenon is a function of n independent variables, then its dimensionless quantity is a function of $n - k$ dimensionless variables, k being the number of fundamental units [92].

In order to perform a dimensional analysis of the droplet speed, v, the variables that have major influence on the final droplet velocity have to be identified. Based on the analysis of metal transfer presented in Section 5.1.3, the welding parameters playing a major role on the formation and detachment of the droplet in pulsed GAMW are: peak, background and mean currents; average arc voltage, V; time at peak current, t_p; pulse frequency, f; and wire feeding speed, s. Changes in pulse parameters will promote changes in the properties of the arc [71, 48] and the metal being transferred [93], and hence in the dynamic balance of the forces acting on droplet formation and detachment. Therefore, arc electrical conductivity, σ, and magnetic permeability, μ_0, and motel metal surface tension

coefficient, should also be included and variables. Also, the droplet radius and density would have to be included in the analysis.

As shown in subsection 2.2.1, the radius of the droplet influences the magnitude of the electromagnetic, momentum flux, drag and surface tension forces, and hence it should be also included. Therefore, based on the analysis of the reported results in subsection 5.1.3 and taking into account the forces acting of droplet transfer (see subsection 2.2.1), droplet velocity, v, will be expressed as a function of the following variables:

$$v = f\left(I_p, I_b, I_m, V, t_p, f, s, \mu_o, \sigma, \rho, \gamma, r\right) \tag{5.1}$$

where:

$I_p =$ peak current $[I]$;

$I_b =$ background current $[I]$;

$I_m =$ mean current $[I]$;

$V =$ average voltage $[ML^2T^{-3}I^{-1}]$;

$t_p =$ time at peak current $[T]$;

$f =$ pulse frequency $[T^{-1}]$;

$s =$ wire feeding speed $[LT^{-1}]$;

$\mu_o =$ permeability constant $[MLT^{-2}I^{-2}]$;

$\sigma =$ arc electrical conductivity $[M^{-1}L^{-3}T^3I^2]$;

$\rho =$ wire density $[ML^{-3}]$;

$\gamma =$ surface tension coefficient $[MT^{-2}]$;

$r =$ droplet radius $[L]$.

The gravitational acceleration, g, was not included as a variable because it has a secondary effect on droplet velocity, when compared to the other forces playing a role. In addition to that, for pulsed GMAW, the droplet speed is greatly influenced by the conservation of momentum of the fluid flow developed inside the forming droplet during peak phase of the current profile [88, 89, 31, 90, 44], which in the case of the present investigation are all above 380 A. Furthermore, in the present study, once the droplet detaches, the gravitational force acting on the droplet can be assumed as equal for both profiles in the range of parameters investigated, given that droplet diameter for all conditions are approximately the same, as shown in Figure 5.7.

In total, there are 12 independent variables, plus the dependent variable droplet velocity, giving a total of 13 variables, $n = 13$. The number of fundamental units involved in this problem is four, $k = 4$: length $[L]$, mass $[M]$, time $[T]$ and current $[I]$. Hence, according to the Buckingham π-theorem, there should be 9 dimensionless numbers, among which eight are independent and the ninth is the dimensionless values of velocity. Following are the nine dimensionless numbers used for the analysis in the present work (their derivation is detailed in Appendix A).

$$\bar{I}_b = \frac{I_b}{I_p} \tag{5.2}$$

$$\bar{I}_m = \frac{I_m}{I_p} \tag{5.3}$$

$$\bar{V} = \frac{I_p V}{\gamma s r} \tag{5.4}$$

$$\bar{t}_p = t_p \frac{s}{r} \tag{5.5}$$

$$\bar{f} = f \frac{r}{s} \tag{5.6}$$

$$\bar{\mu}_o = \frac{\mu_o I_p^2}{\gamma r} \tag{5.7}$$

$$\bar{\sigma} = \frac{\sigma \gamma s r^2}{I_p^2} \tag{5.8}$$

$$\bar{\rho} = \frac{\rho r s^2}{\gamma} \tag{5.9}$$

and then the dimensionless velocity, $\bar{v}$, is

$$\bar{v} = \frac{v}{s} \tag{5.10}$$

It was verified during the NN training and testing step that, if instead of expressing the dimensionless droplet velocity as in Equation 5.10, it is represented as Equation 5.11 such that the trained model predictability is enhanced.

$$\bar{v} = \sqrt{\frac{v}{s}} \tag{5.11}$$

Regardless of which dimensionless velocity is used, either Equation 5.10 or 5.11, the dimensionless velocity can be expressed as a function of the dimensionless independent variables as follows

$$\bar{v} = \psi\left(\bar{I}_b, \bar{I}_m, \bar{V}, \bar{t}_p, \bar{f}, \bar{\mu}_o, \bar{\sigma}, \bar{\rho}\right) \tag{5.12}$$

From that, it follows that if the value of the ψ function is estimated according to Equation 5.10, the dimensional droplet speed can be found to be equal to

$$v = s \times \bar{v} \tag{5.13}$$

or

$$v = s \times \bar{v}^2 \tag{5.14}$$

if Eq. 5.11 is used as the dimensionless value of droplet velocity.

The dimensional groups presented above were used as inputs in the *MLP Regressor* NN algorithm. During the training exercise, it was verified that the algorithm parameters that more strongly affect the predictive capability of the model, as measured by the Pearson correlation coefficient, was the number of nodes (neurons) in the hidden layer and folds used for cross validation. Varying the number of hidden nodes and the number of cross-validation folds (procedure detailed in Appendix B), it was determined that 1 hidden node

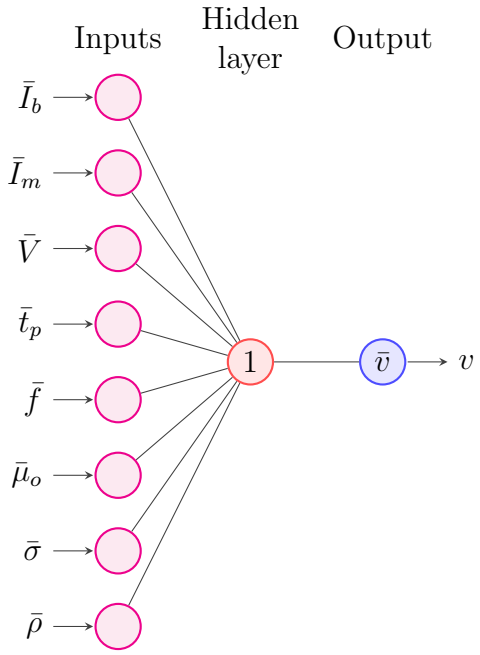

Figure 5.9: Neural network diagram.

and 10 cross-validation folds yield the highest Pearson's correlation coefficient and lower variability. Indeed, 10-folds cross validation is reported in the literature as an optimum number for minimization of prediction error [85, 86, 94, 95]. Figure 5.9 shows schematically the NN diagram used. Cross validation using 10-folds, means that the dataset is divided into 10 equal parts, then 9 of them were used for training, then the trained model is tested on the one instance left. After that, 9 different instances, including the one that was left aside in the previous iteration, are used for training and then the trained model is tested on the one instance left aside in at this iteration. In the end, all 10 instances were used exactly one time for testing. The remaining NN parameters were, ridge equal to 0.01, seed equal to 1 and tolerance of 10^{-6}. For the purpose of verifying the trained model, a set of data, not used in training step, was used for testing the trained model. Those are indicated by filled stars, "★".

Table 5.2 shows the trained model statistics and Table 5.3 presents the statistics of testing when the set of 6 droplet velocity data points was used as a test set. It can be seen

Table 5.2: Neural network training statistics for a set of 30 droplet velocity data.

Statistics	Model 1	Model 2
Correlation coefficient	0.8971	0.9112
Mean absolute error	1.5780	0.2313
Root mean squared error	1.8765	0.2726
Relative absolute error	42.69%	40.45%
Root relative squared error	42.42%	39.48%

Table 5.3: Neural network model testing statistics for 6 random droplet velocity data.

Statistics	Model 1	Model 2
Correlation coefficient	0.9895	0.9918
Mean absolute error	0.9695	0.1304
Root mean squared error	1.1278	0.1522

that both trained models yielded high correlation coefficients when tested on the 6 data points. In Fig. 5.10 the predicted droplet velocity are plotted against the measured values for both models. The dashed lines represent the 95% upper and lower prediction bounds of the trained models, i.e. model prediction interval. Note the testing points falling inside the model prediction internal over the equality line, as indicated by the filled star, "★", confirming the predictive generality of the trained models.

Another way to compare predicted to measured values is by using the Bland-Altman plot [96]. On this plot, the difference between measured and predicted values are plotted against their average. The central solid horizontal line is equal to the mean of the difference and represents the bias between measurements and predictions, and hence the closer this value is to zero, the lower is the bias and better is the agreement between predicted and measured values. This method also makes the assumption that, if the residuals between measured and estimated are normally distributed, 95% of them should fall in the interval between $\pm 1.96\,\mathrm{SD}$, where SD is the standard deviation of the differences. Therefore, this plot is able to show what is the bias between measured and estimated droplet velocity values, and the range in which 95% of the residuals are included. The Bland-Altman plots are presented in Fig. 5.11. From those plots it can be seen that both models give low bias, and based on margin of error bounded by $\pm 1.96\,\mathrm{SD}$, it can be affirmed that the

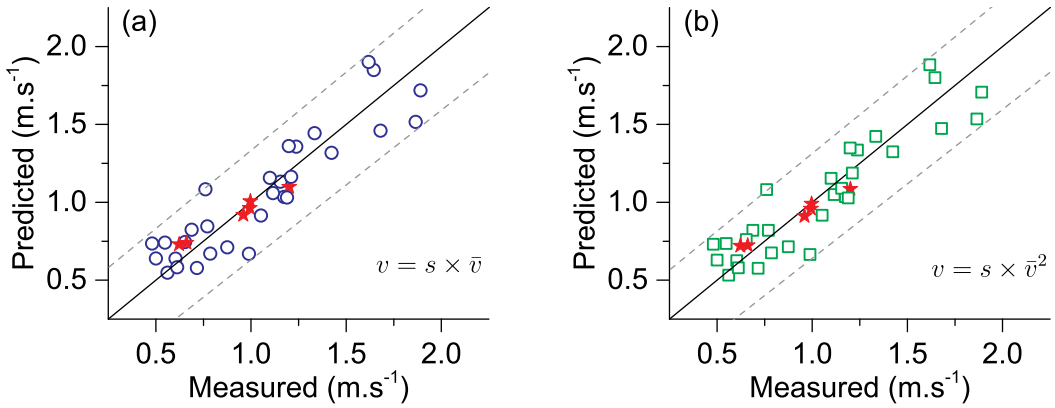

Figure 5.10: Measured and predicted droplet velocity for the different models. The set of random experiment are represented by (★) symbol, and are the same used to investigate the influence of peak and background current on the velocity of the droplet and is shown on Fig. 5.8.

trained models the capability of predicting droplet speed within a margin of error of about $\pm 0.33\,\mathrm{m.s^{-1}}$.

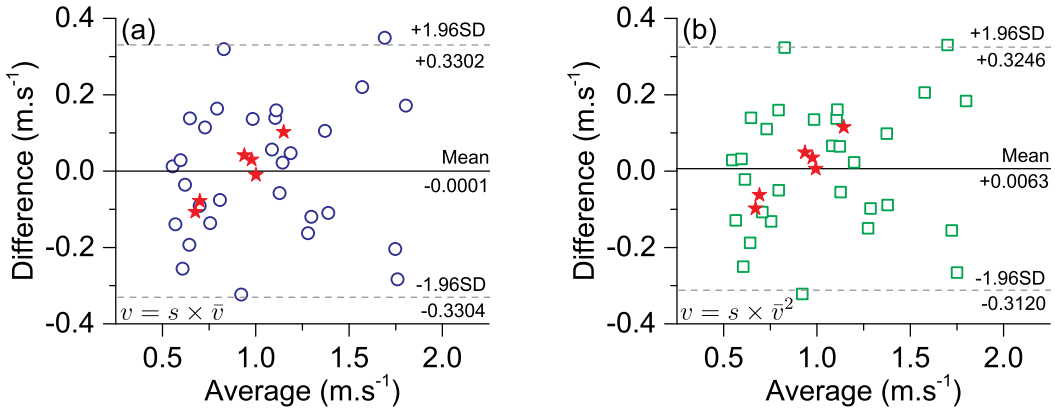

Figure 5.11: Bland-Altman plot for the measured and predicted droplet velocity. The set of random experiment are represented by (★) symbol, and are the same used to investigate the influence of peak and background current on the velocity of the droplet and is shown on Fig. 5.8.

MLPRegressor classifier was chosen because it has just one hidden-layer, leading to

a simpler algorithm, that has capabilities to be incorporated into embedded systems, as it is used in other fields, as for example in medicine for tracking physical health of individuals [97]. Regarding its applicability to welding, the methodology described here, at an advanced stage, could be used for training of models capable of predicting bead penetration, which then could be embedded into welding power supplies to estimate bead penetration by using the process parameters as input, or even in mobile devices that can be used in the field by welding engineers and practitioners.

5.2 Bead characteristics[2]

5.2.1 Bead penetration

In Figure 5.12 the bead total penetration is plotted against wire feeding speed and welding heat input, for both profiles at different wire feeding speeds and pulse settings. Note that profile 1, at low I_b/I_p pulse setting, exhibits the highest bead penetration compared to all other profiles, while profile 2 at low T_b/I_p current setting presented the lowest bead penetration values. Note also the good correlation between bead penetration and welding heat input, suggesting that the lower penetration for profile 2 is related to the lower heat input that this profile required to transfer metal, compared to profile 1.

Figures 5.13 and 5.14 presents the bead cross section for the wire feeding speed of 200 and 300 ipm, respectively. From the bead cross sections, one can see that the high penetration of profile 1 with the settings of low I_b/I_p current ratio has mainly a finger-like penetration profile, see Figures 5.13(c) and 5.14(c). This penetration profile is a characteristic resulting from the impact of the high speed impinging droplet (see Figure 5.7), and consistent with the trend reported by Essers and Walter [8], in which the depth of

[2]The contents of this section of the chapter have been incorporated within an article available in the Proceedings of the 10th International Conference on Trends in Welding Research & 9th International Welding Symposium of Japan Welding Society (9WS), October 11-14, 2016, Tokyo, Japan, organized by American Welding Society (AWS) & Japan Welding Society (JWS), pages 579-583. E. B. F. Dos Santos, A. R. H. Midawi, R. Pistor and A. P. Gerlich, "Influence of pulse profile on droplet transfer dynamics and its implication on gas metal arc weld bead penetration and cooling rate".

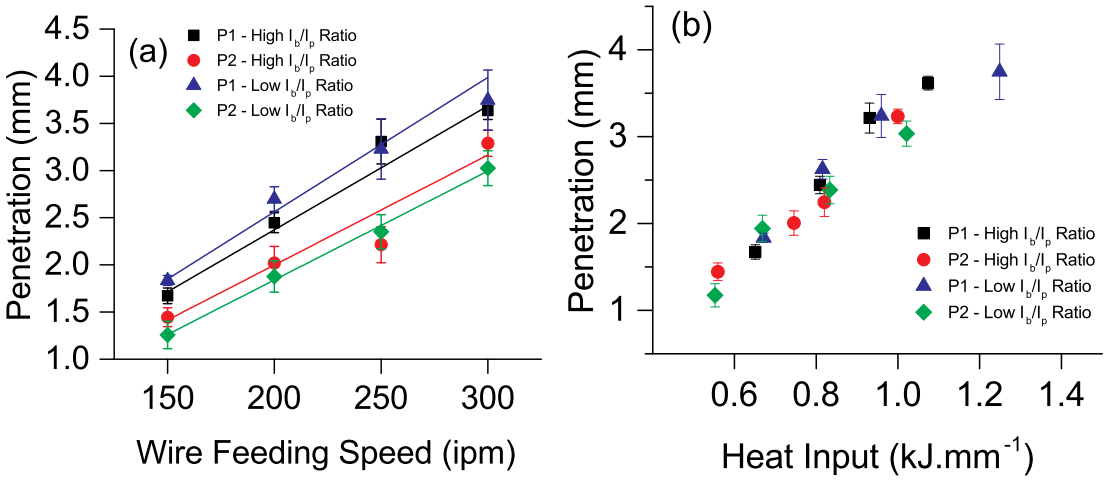

Figure 5.12: Variation of bead penetration for different pulse profiles with (a) wire feeding speed and (b) heat input.

penetration is mostly influenced by the impact of the impinging droplet, while the bead total cross-sectional area is a consequence of the heat content of the impinging droplet.

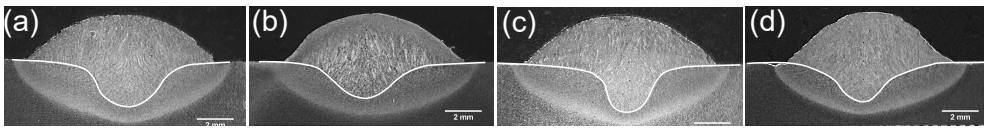

Figure 5.13: Bead cross section for the wire feeding speed of 200 ipm for (a) profile 1 with high I_b/I_p, (b) profile 2 with high I_b/I_p, (c) profile 1 with low I_b/I_p and (d) profile 2 with low I_b/I_p current ratio.

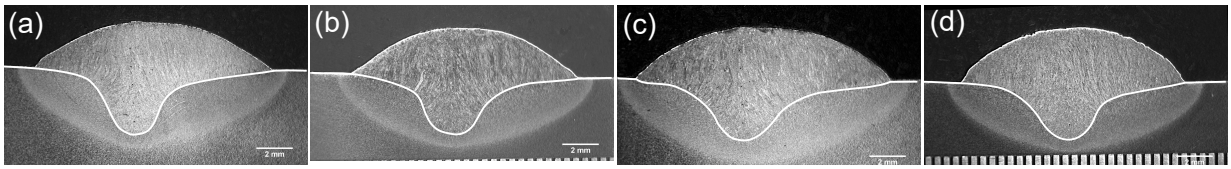

Figure 5.14: Bead cross section for the wire feeding speed of 300 ipm for (a) profile 1 with high I_b/I_p, (b) profile 2 with high I_b/I_p, (c) profile 1 with low I_b/I_p and (d) profile 2 with low I_b/I_p current ratio.

Figure 5.15 shows the overlap of bead penetration profiles, for the wire feeding speed of

200 ipm. One can see that profile 1 produces the greatest penetration, and that the setting of low I_b/I_p current ratio leads to a smaller total penetrated cross-sectional area compared to high I_b/I_p current ratio setting. Consistently, profile 2 with high I_b/I_p current ratio setting provides the lowest penetration and a larger total penetrated cross-sectional area, when the opposite is true when comparing to low I_b/I_p current ratio setting. In section 5.1.2 it was shown that droplet detachment for profile 2 occurs at background current values, compared to detachment when using a higher current for profile 1, suggesting that the heat content of the droplet of profile 2 is lower, and this is supported by the lower penetration for profile 2. For the wire feeding speed of 200 ipm the droplet velocity, and diameter was the same for both profiles at the different settings.

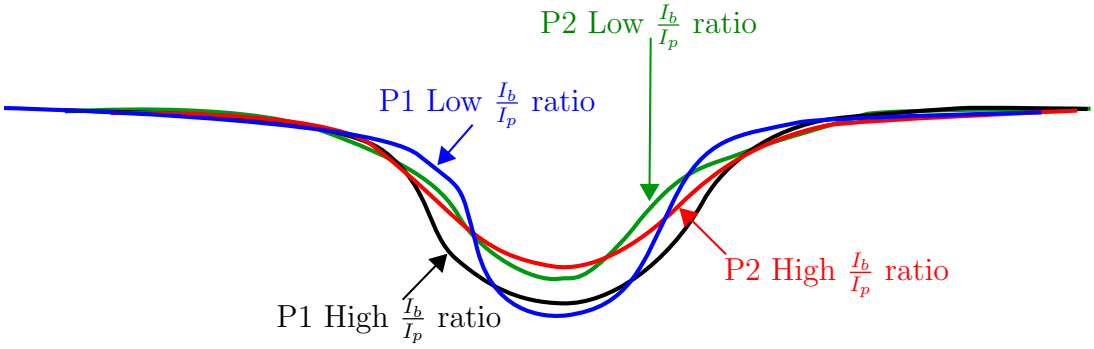

Figure 5.15: Comparison of penetration profile for the wire feeding speed of 200 ipm.

In Figure 5.16 bead penetration is plotted against the momentum rate and effective momentum, and one can see that neither of the quantities presents a clear correlation to bead penetration, as it have been reported by previous researchers [8, 9]. The lack of correlation between bead penetration and momentum rate and effective momentum for the case of GMAW-P is due to the fact that, the momentum quantities take into consideration only mass transfer, and not necessarily the heat transfer. The authors that reported a good relationship between those quantities, were investigating for constant voltage GMAW where droplet speed and detachment frequency is proportional to average current, and hence droplet heat content carried by the droplet [36, 37]. However as shown in subsection 5.1.3 that is not the case in GMAW-P, where the droplet speed and detachment frequency is not necessarily proportional to the average welding current, and hence the correlation does not hold.

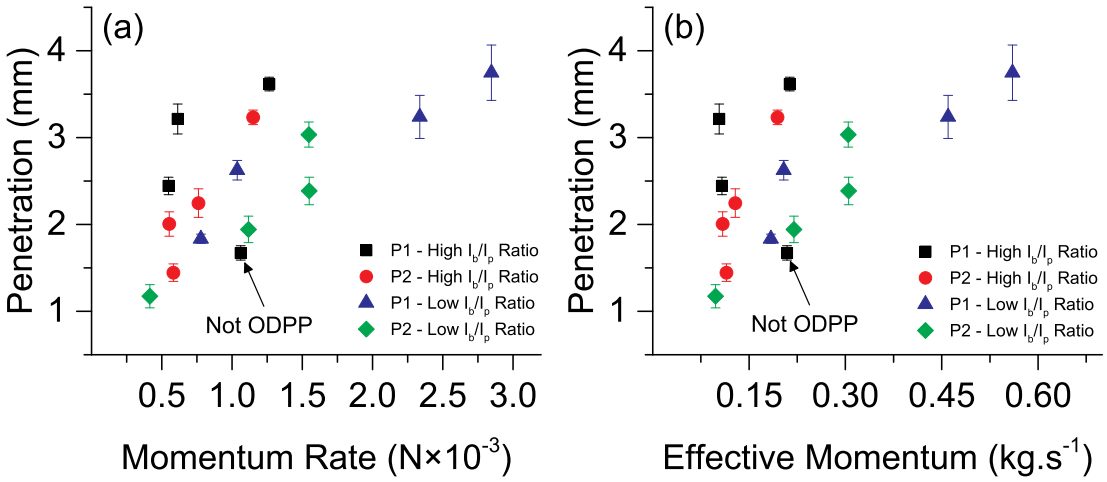

Figure 5.16: Correlation between bead penetration and (a) momentum rate [8] and (b) effective momentum [9].

Using dimensional analysis, Murray and Scotti [10] modelled bead penetration as a function of mass and heat transfer dimensionless number, A and B respectively. In Figure 5.17 those dimensionless numbers are plotted against wire feeding speed for each profile and pulse setting. From Figure 5.17(a) it is noted that the mass transfer number changes slightly between the profiles for a given wire feeding speed, and that it increases with wire feeding speed, owing to increased wire feeding rate. On the other hand, as shown in Figure 5.17(b), the heat transfer number is higher for profile 1 using high I_b/I_p current ratio, and the lowest for profile 2 using low I_b/I_p current ratio.

In Figure 5.18 penetration is plotted as function of mass and heat transfer coefficients and heat input. If one considers the penetration as a function of the dimensional number only, it can be seen that for the same mass transfer number, bead penetration is deeper for profile 1, compared to profile 2, see Figure 5.18(a), owing to the lower heat transfer number of profile 2. The variation of penetration as a function of heat transfer number is shown in Figure 5.18(b), and one finds that penetration increases with heat transfer number, and that for a given heat transfer number, profile 1 with low I_b/I_p current ratio setting have the highest penetration. This is a consequence of the high droplet velocity which increases the momentum rate and/or effective momentum (Figure 5.16), explaining

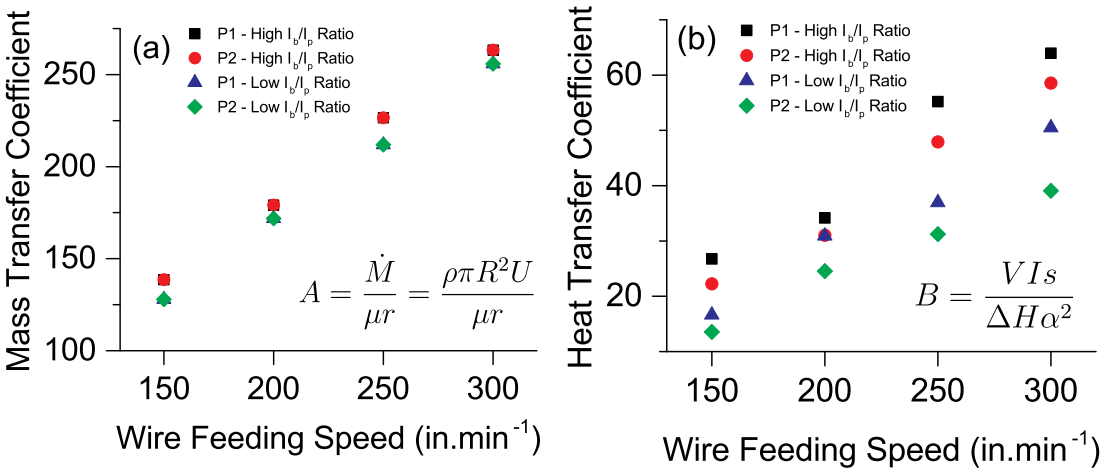

Figure 5.17: Variation of (a) mass and (b) heat transfer numbers with wire feeding speed for profiles 1 and 2 for the different settings investigated.

the lowest penetration for profile 2 when a low I_b/I_p current ratio is used, given that it has lowest mass and heat transfer numbers, as well as low droplet velocity.

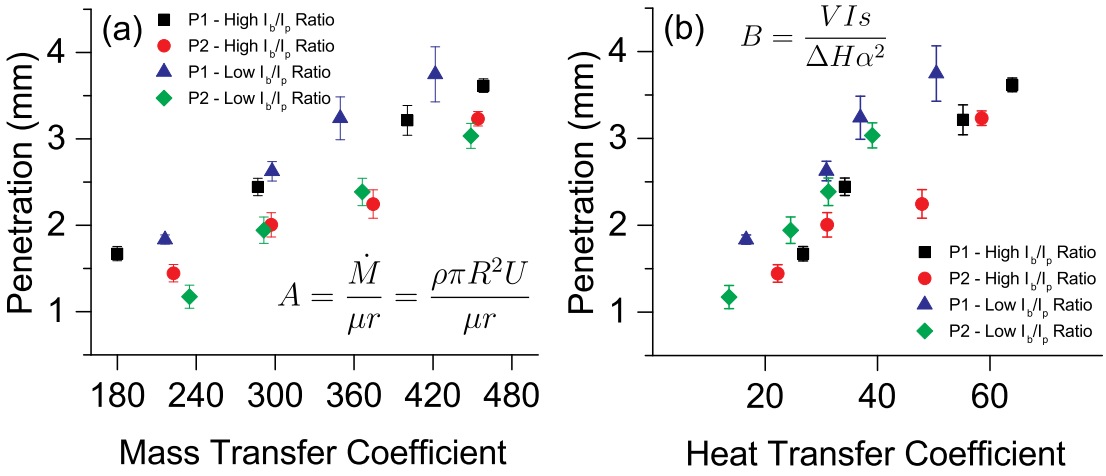

Figure 5.18: Variation of penetration with (a) mass (b) heat transfer numbers.

Bead penetration was predicted according to the model proposed by Murray and Scotti [10] and the comparison between predicted and measured values is shown in Fig-

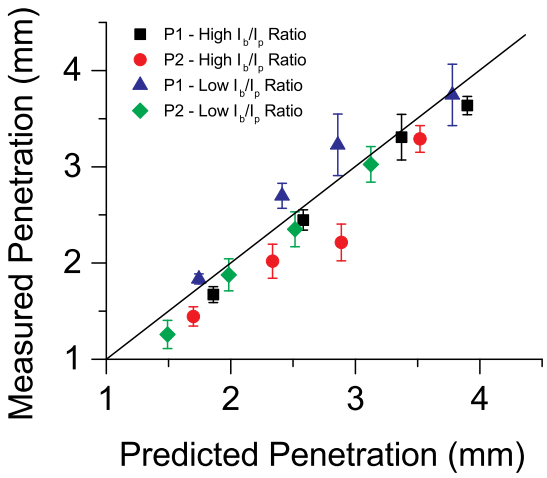

Figure 5.19: Comparison of measured and predicted penetration according to the model proposed by Murray and Scotti [10].

ure 5.19. Although it is possible to see some agreement between predicted and measured values, a closer analysis reveals that in overall the model predicted values is lower that the measured one for pulse 1 with low I_b/I_p current settings. Note that this is the condition where faster droplet speeds are achieved, and hence the model does not take the droplet velocity into account, and so the predicted values are smaller.

The results of this section suggests that in order to model bead penetration, a model should take into account the transfer of mass, heat and momentum from the transferring droplet. Furthermore, for GMAW-P droplet speed should be directly included into the model and not indirectly by means of average current, given that in GMAW-P droplet speed is not necessarily proportional average welding current.

5.2.2 HAZ characteristics

As discussed in previous sections, profile 2 transfer metal required the least amount of arc power. This can also imply in lowering the heat content provided to the base metal, what can be an advantage when welding heat sensitive materials. To evaluate whether or not there is a difference in the amount of heat given to the base metal, the HAZ area and

prior austenite grain size in the coarse grain heat affected zone (CGHAZ) was measured. Figure 5.20 compares the HAZ area and prior austenite grain size in the CGHAZ for

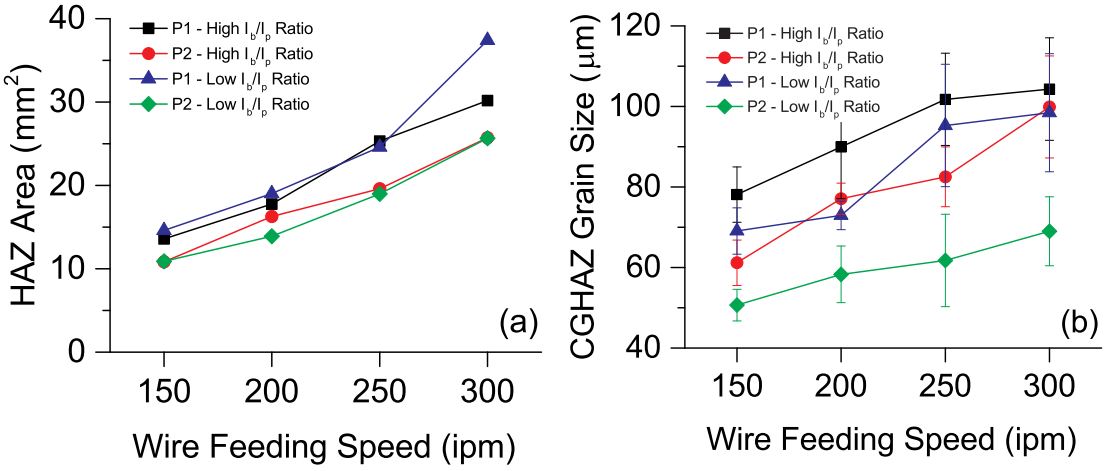

Figure 5.20: (a) HAZ area and (b) CGHAZ prior austenite grain size.

both profiles at the different settings evaluated. It is observed that the HAZ area is in fact smaller when profile 2 is used, Figure 5.20(a). The measurements reveals that the apparent prior austenite grain size is smaller for profile 2 when using a low I_b/I_p current ratio setting, Figure 5.20(b). This can be understood as a lower peak temperature, due to the lower heat input to the base metal, consequently reducing the amount of growth of the austenite grain in the regions above astenitization temperature. Despite the scatter in the measurements of HAZ characteristics, these results, in addition to the analysis of penetration presented in section 5.2.1, confirm that the metal transfer for profile 2, can be achieved such that the amount of heat input to the base metal can be reduced.

Chapter 6

Streaming transfer: the metal beam[1]

Overview

This chapter presents the characteristics of a streaming transfer that is achieved at low arc lengths. The metal transfer occurs when using a nearly square shaped current profile, profile 2, such that when high pulse frequency are used with high peak and low background current, a stream metal transfer is achieved with a short arc lengths.

6.1 The metal beam

The comparison of metal transfer between profiles 1 and 2, as presented in sections 5.1.1 and 5.1.2, is summarized in Figure 6.1. This shows that the droplet is not yet completely formed when pulse assumes a background current value for profile 2, specially when high peak and low background currents are used (low I_b/I_p current ration setting). It can be seen that for profile 2 (P2) the minimum diameter of the necking region is larger compared

[1]The content of this chapter have been incorporated within an Accepted Manuscript of an article published by Elsevier B.V. in *Manufacturing Letters* on January 5, 2017, available online: http://www.sciencedirect.com/science/article/pii/S2213846317300019. E. B. F. Dos Santos, R. Pistor and A. P. Gerlich, "High frequency pulsed gas metal arc welding (GMAW-P): the metal beam process".

to that of profile 1 (P1). Furthermore, when using profile 1, most of droplet formation and detachment happens before the background current is achieved. For example on Figure 6.1, at a wire feeding speed of 300 ipm, the droplet has already completely detached for profile 2, Fig. 6.1(d), while for profile 2 the droplet is still at an early stage of formation, Fig. 6.1(h).

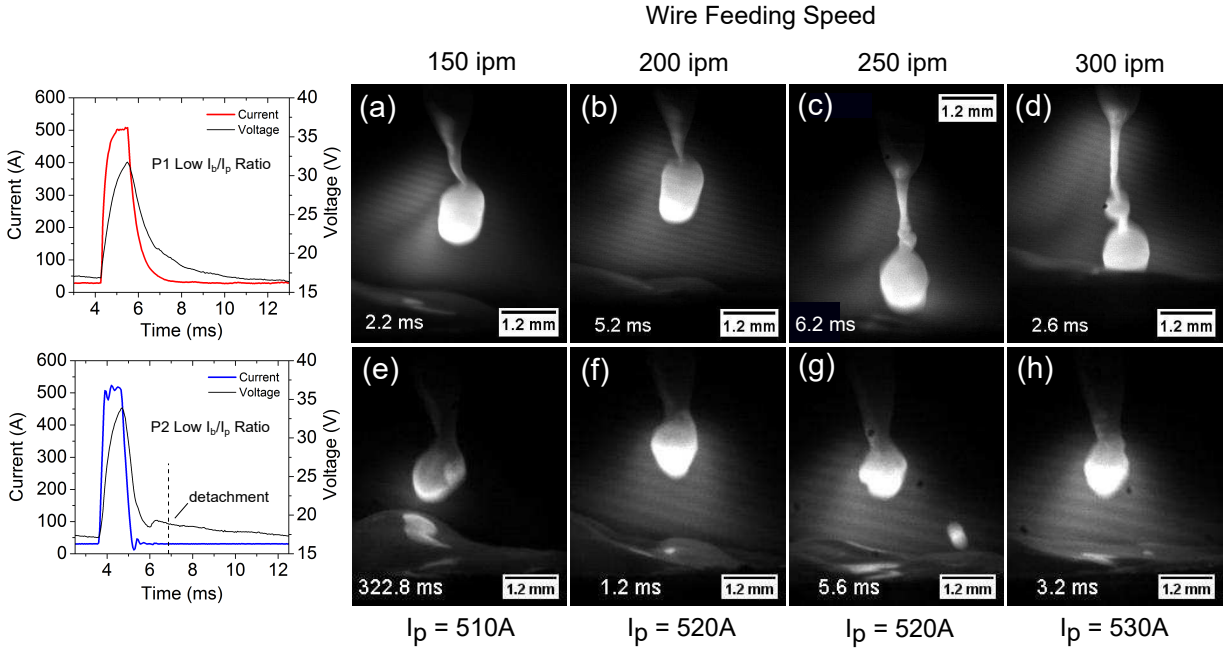

Figure 6.1: These figures shows the droplet shape at the moment that background current value is reached, for the same wire feeding speed equal values of peak and background current and pulse frequency were used for the different profiles according to shown in Table 4.1.

This observed difference in the sequence of droplet formation, indicated that it would be possible to achieve a continuity in the constricted region of the wire when profile 2 is used, possibly by increasing the frequency of the current pulse. Indeed the streaming transfer was achieved with travel and wire feeding speeds of 30 ipm (0.76 m.min^{-1}) and 550 ipm (13.97 m.min^{-1}), respectively. Peak and background current were of 550 A and 50 A, respectively. The pulse frequency was varied from 300 to 600 Hz, in steps of 100 Hz, and the duty cycle for each frequency was of 45.4, 45.9, 46.2 and 47.1 %, respectively. With

this optimum combination of parameters, it was possible to achieve a streaming transfer of molten metal, hereafter refereed as "metal beam", and it is shown in Figure 6.2 for the frequency values of 300, 400, 500 and 600 Hz.

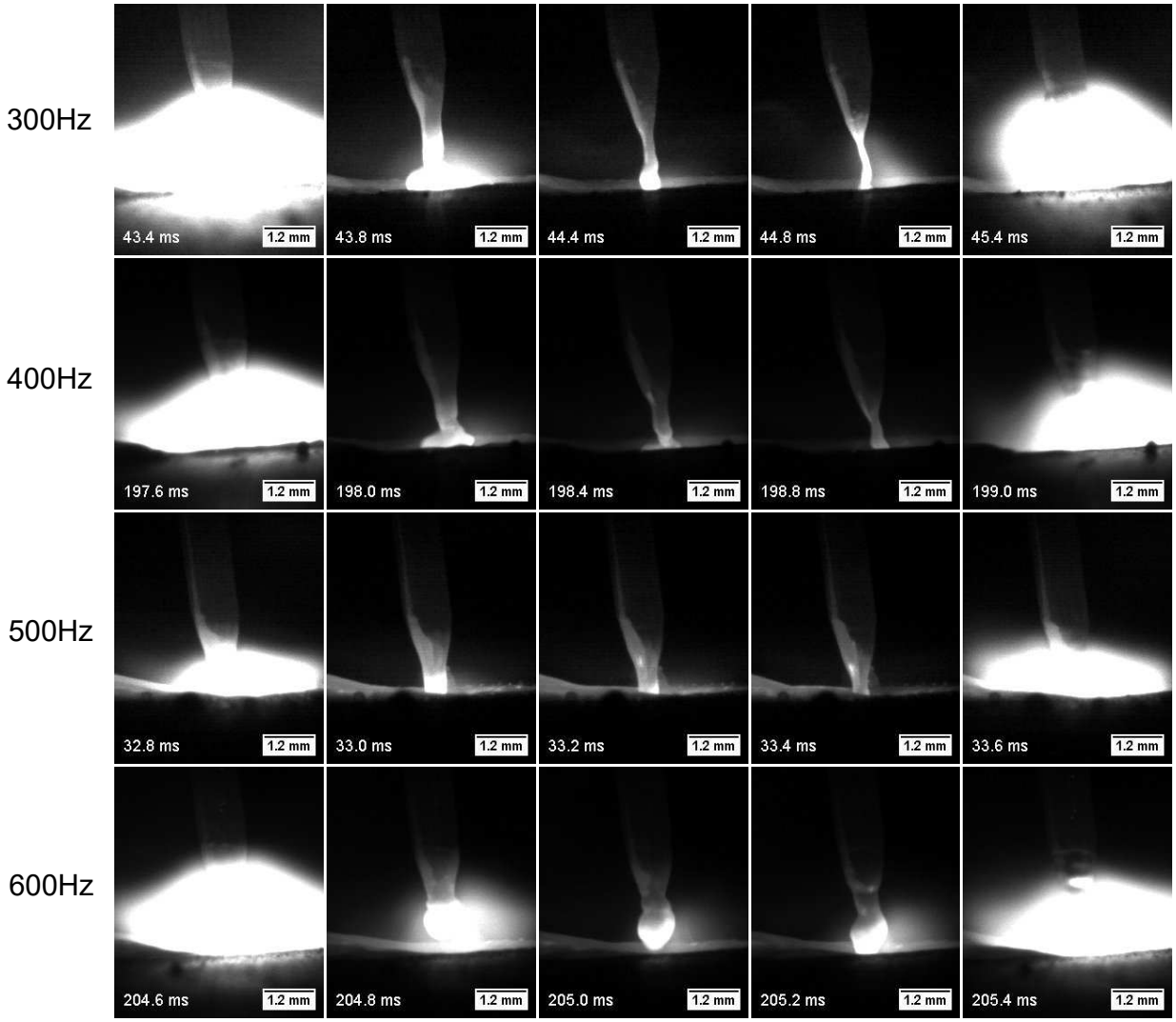

Figure 6.2: Effect of pulse frequency on metal beam shape and stability.

As shown on Figure 6.2, for fixed values of the current pulse and travel speeds, changing the pulse frequency will influence the uniformity of the streaming transfer and the metal

beam stability. Note the increase in the diameter of the metal beam, at the moment prior to the beginning of the next cycle (second last column of each line), as the pulse frequency increases. Furthermore, Figure 6.2 shows that, compared to the optimum pulse frequency, lower frequencies permit the breakdown of the beam of metal before the onset of the next pulse. On the other hand, if the frequency is higher than the optimum values, the time at the peak current is not sufficient to melt and constrict the wire, and therefore short circuits can occur, promoting instability of the metal transfer. This suggests that the higher the frequency the higher peak current are needed along with lower base current values are required.

Additionally, even though the values of peak and background current were set the same, one can observe a variation in the visible arc length during the peak phase of current as the pulse frequency changes (corresponding to the first column of Figure 6.2). The visible arc length decreases as the pulse frequency changed from 300 to 500 Hz and then increases again at 600 Hz. This distance was measured for 20 cycles and at the peak current, corresponding to the maximum arc length, and the results are shown on Table 6.1. As observed from Figure 6.2, the measurements in Table 6.1 confirm a decrease of arc length to a minimum value, at a frequency of 500 Hz, and then an increase at a frequency of 600 Hz. The increase in arc length for frequency values below 500 Hz can be due to the break-down of the beam of molten metal, therefore allowing a longer arc gap at the moment that the new pulse is initiated. Likewise, the longer visible arc length for the frequency of 600 Hz is due to the establishment of a gap between the electrode tip and weld pool.

Table 6.1: Influence of pulse frequency on average voltage, current, nominal heat input, arc length and beam transfer stability.

Frequency (Hz)	Voltage (V)	Current (A)	Heat Input (kJ/mm)	Arc length (mm)	
				Average	Variance
300	24.8	276.9	0.54	2.71	0.205
400	25.8	279.6	0.57	2.15	0.045
500	26.3	281.2	0.58	1.77	0.005
600	26.9	285.5	0.61	2.52	0.010

Table 6.1 also gives the variance of arc length at peak current. This value gives a direct

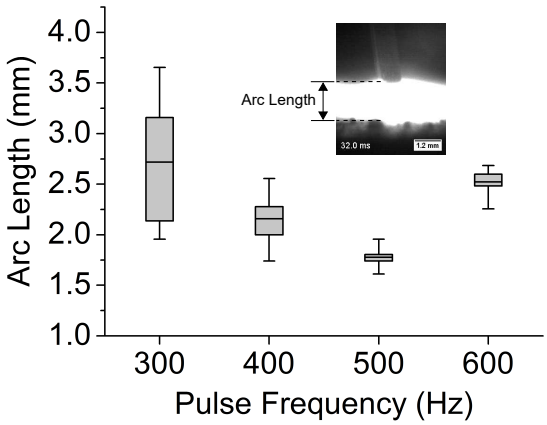

Figure 6.3: Influence of pulse frequency on the visible arc length and stability.

indication of the scatter in the measurements, and hence provides information about the regularity of the maximum arc length for the range of frequencies reported. It can be seen that for this set of parameters, the frequency of 500 Hz has the shortest arc length, and the smallest variance, which signifies a more stable setting for the streaming transfer. This was also supported by the electrical signal measured, which revealed no short-circuit events (voltages < 1 V) occurring over a 2 s period using these conditions. This is best seen graphically in Figure 6.3, which shows a whiskers plot of the data reported in Table 6.1. For each frequency, the limits of the whiskers corresponds to the variation range given by the maximum and minimum measured values and the central line is the mean value. Therefore, this indicates that there will be an optimum set of parameters for which a regular stream transfer can be achieved with a stable maximum arc length smaller than 2 mm.

6.2 Significance of results

The streaming transfer described here was achieved even though pure argon or argon plus oxygen mixture have not been used as a shielding gas, which is usually a condition for achieving stream transfer with a constant voltage GMAW [50, 51]. Additionally, the metal stream did not appear to rotate, which differentiates this transfer mode from the rotating

spray mode when using constant voltage GMAW [50, 51], and the stability of the metal stream can be attributed to the high frequency current pulse, which helps to maintain the beam straight as shown in Fig. 6.2.

This transfer mode can be optimized for applications where short arcs are required such as narrow groove filling in the joining of high strength low alloy (HSLA) steels with high productivity, while maintaining a low occurrence of spatter. The short arc achieved can also potentially reduce the fume formation rate, however further work is needed to confirm this. Notice from Table 6.1 that a stable streaming (spatterless) transfer was accomplished at a wire feeding speed of 550 ipm (13.97 $\mathrm{m.min^{-1}}$) with heat input as low as 0.58 $\mathrm{kJ.mm^{-1}}$.

Considering the wire feeding speed used and the short arc length achieved, this metal transfer mode provides an option for high productivity welding process with potential advantages for narrow groove welding of heat sensitive materials.

Chapter 7

Concluding remarks and recommendations for future research

In this chapter a comprehensive conclusion, based on the results gathered during the investigation, is made. Following that, suggestions of future work are proposed.

7.1 Comprehensive conclusion

The influence of two current pulse profiles and pulse parameters on metal transfer in pulsed gas metal arc welding droplet have been investigated by means of high speed imaging and analysis of electrical signals. Droplet formation and transfer was compared between both profiles for different welding process parameters.

One pulse profile had a long tail exponential shape (profile 1) and the second had a nearly square shaped (profile 2). The metal transfer was analyzed in terms of droplet formation and detachment. The results showed that for the profile using a long tail current transition, most of droplet formation and detachment occurs before background current is reached. On the other hand, for the nearly square pulse, most droplet formation and transfer occurs during background current. By decreasing the transition time from peak to background current, the necking diameter of the constricted wire is larger when background

current is achieved. It was also found that when high peak and low background current are used (i.e. with low I_b/I_p ratios) most melting and droplet formation occurs during peak phase of current, considering the droplet already formed when the pulse assumes background current.

One of the main findings of this work is that droplet detachment is found to differ for the investigated profiles. For profile 1 the arc attaches to the constricted region of the wire during the transition from peak to background current, while for profile 2 the arc keeps attached to the bottom of the the forming droplet and only after detachment occurs the arc attaches to the wire necking region. This jump in arc attachment position was detected by monitoring the voltage signal and confirmed using high speed photography.

Another conclusion of this investigation is that droplet speed was found to be faster the lower the ratio between base to peak current, I_b/I_p. It was found that the faster speed is not only due to the larger peak current, but also due to the lower background current, which reduces the arc pressure prior to droplet detachment. Additionally, for the same wire feeding speed, droplet speed is not proportional to the average current, as opposed to that observed in constant voltage GMAW. A neural network model was trained to predict droplet speed, using as input parameters dimensionless groups. Despite the reduced amount of data available, the trained models have the capability of predicting droplet speed within a 95% confidence interval of $\pm 0.33\,\mathrm{m.s^{-1}}$.

It was also found that, the nearly square shape pulse profile requires lower arc power to transfer metal in the one droplet per pulse, when compared to the second profile investigated. This was a influence in the total bead penetration and heat input to the base metal. The correlation between bead penetration and the momentum of the impinging droplet was not as good as it is for constant voltage GMAW.

Stable streaming metal transfer was achieved using a wire feeding speed of around 14 $\mathrm{m.min^{-1}}$ and travel speed of $0.762\,\mathrm{m.min^{-1}}$, with a resulting heat input of $0.58\,\mathrm{kJ.mm^{-1}}$. Additionally, this metal transfer was achieved with a short arc length of less than 2 mm. This transfer mode is promising for joining heat sensitive materials, given the low heat input values.

7.2 Suggestion for future work

From the observations of the present work, the need for further studies is required in order to have a comprehensive understanding of the metal transfer mechanism. The following list of investigations may be carried out in order to allow the optimization of each pulse profile, so that each of them can be used at their best process conditions and for specific applications:

- First, a fundamental study, using numerical simulation and experimental techniques such as optical emission spectroscopy, is required to quantify the amount of metal vapor for the different profiles.
- As the results suggested that for a given wire feeding speed, when the same welding parameters are used, the amount of iron metal vapor generated differ between the profiles. A study on fume generation would clarify if this in fact represent changes in the amount of welding fume generated by the two pulse profiles.
- The streaming metal transfer introduced in Chapter 6 have to be investigated for a wider range of process parameters, including the influence of pulse frequency, peak and background current, and duty cycle. This study should also consider difference shielding gases and material systems, such as aluminum and magnesium alloys.
- The application and performance of the streaming transfer in the joining of heat sensitive materials, such as high strength low alloy steels, have to be considered.
- Experiments for a wider range of process parameters would build a more reliable model to predict droplet speed and bead penetration.

References

[1] D. R. Schilling, "World's Largest Ship Ever Built and First Floating Liquefied Natural Gas (FLNG) Platform to Begin Drilling in 2017," 2014. xii, 2

[2] P. P. Alexander, "Method and Apparatus for Arc Welding," 1924. xii, 6, 7

[3] N. Arif, J. H. Lee, and C. D. Yoo, "Modelling of globular transfer considering momentum flux in GMAW," *Journal of Physics D: Applied Physics*, vol. 41, p. 195503, oct 2008. xii, 9, 10, 45

[4] S.-F. Goecke, *Auswirkungen von Aktivgaszumischungen im vpm-Bereich zu Argon auf das MIG- Impulsschweißen von Aluminium.* Doctoral thesis, Technischen Universität Berlin, 2005. xii, 13, 14, 15

[5] M. E. Rouffet, M. Wendt, G. Goett, R. Kozakov, H. Schoepp, K. D. Weltmann, and D. Uhrlandt, "Spectroscopic investigation of the high-current phase of a pulsed GMAW process," *Journal of Physics D: Applied Physics*, vol. 43, p. 434003 (9pp), nov 2010. xii, 15, 16, 41

[6] Y. Ogino, Y. Hirata, and A. B. Murphy, "Numerical simulation of GMAW process using Ar and an ArCO2 gas mixture," *Welding in the World*, vol. 60, pp. 345–353, mar 2016. xii, 15, 16, 17, 18

[7] K. Nomura, K. Kataoka, K. Mimura, Y. Hirata, and T. Kishi, "Tomographic spectroscopic observation of argon and metal vapor behavior in MIG arc welding," *Welding in the World*, vol. 60, no. 1, pp. 117–125, 2016. xiii, 15, 17, 19

[8] W. G. Essers and R. Walter, "Heat transfer and penetration mechanism in GMAW and Plasma-GMA welding," *Welding Journal*, vol. 60, no. 2, pp. 37s–42s, 1981. xiii, xv, 17, 20, 22, 57, 59, 60

[9] A. Scotti and C. Rodrigues, "Determination of momentum as a mean of quantifying the mechanical energy delivered by droplets during MIG/MAG welding," *The European Physical Journal Applied Physics*, vol. 45, p. 11201, jan 2009. xiii, xv, 7, 17, 18, 20, 21, 22, 59, 60

[10] P. E. Murray and A. Scotti, "Depth of penetration in gas metal arc welding," *Science and Technology of Welding and Joining*, vol. 4, no. 2, pp. 112–117, 1999. xv, 7, 20, 60, 61, 62

[11] Shell, "Prelude floating liquefied natural gas (FLNG)," 2017. 1

[12] CEPA, "Let's talk about pipelines - Real conversation about Canada's energy industry," tech. rep., Canadian Energy Pipeline Association (CEPA), 2016. 1

[13] D. B. Rosado, W. D. Waele, and D. Vanderschueren, "Latest developments in mechanical properties and metallurgycal of high strenght line pipes," *Sustainable Construction and Design*, vol. 4, no. 1, pp. 1–10, 2013. 1

[14] W. Cao, M. Zhang, C. Huang, S. Xiao, H. Dong, and Y. Weng, "Ultrahigh Charpy impact toughness (˜450J) achieved in high strength ferrite/martensite laminated steels," *Scientific Reports*, vol. 7, p. 41459, feb 2017. 2

[15] S. Felber, "Welding of the high Grade Pipeline-Steel X80 and Description of Different Pipeline-Projects," *Welding in the World*, vol. 52, pp. 19–41, may 2008. 2

[16] H. H. Wang, K. M. Wu, X. W. Lei, and Y. Qian, "Effect of fast cooling process on microstructure and toughness of heat affected zone in high strength pipeline steel X120," *Science and Technology of Welding and Joining*, vol. 17, pp. 309–313, may 2012. 7, 12

[17] R. Cao, J. Li, D. S. Liu, J. Y. Ma, and J. H. Chen, "Micromechanism of Decrease of Impact Toughness in Coarse-Grain Heat-Affected Zone of HSLA Steel with Increasing

Welding Heat Input," *Metallurgical and Materials Transactions A*, vol. 46, no. 7, pp. 2999–3014, 2015. 2

[18] W. Thomas, P. Threadgill, and E. Nicholas, "Feasibility of friction stir welding steel," *Science and Technology of Welding and Joining*, vol. 4, no. 6, pp. 365–372, 1999. 3

[19] J. W. Sowards, T. Gnäupel-Herold, J. David McColskey, V. F. Pereira, and A. J. Ramirez, "Characterization of mechanical properties, fatigue-crack propagation, and residual stresses in a microalloyed pipeline-steel friction-stir weld," *Materials & Design*, vol. 88, pp. 632–642, 2015. 3

[20] R. Rai, A. De, H. K. D. H. Bhadeshia, and T. DebRoy, "Review: friction stir welding tools," *Science and Technology of Welding and Joining*, vol. 16, no. 4, pp. 325–342, 2011. 3

[21] J. C. Needham, "Pulsed Current for Gas Shielded Arc Welding," *IEEE Transactions on Industry and General Applications*, vol. IGA-2, pp. 225–233, may 1966. 3, 13

[22] E. P. Vilkas, "Square-Wave Welding," *IEEE Transactions on Industry and General Applications*, vol. IGA-3, pp. 525–530, nov 1967. 3

[23] Lincoln Electric, "Surface Tension Transfer (STT)," 2005. 3, 13

[24] Fronius, "CMT: Cold Metal Transfer," 2013. 3, 13

[25] W. J. Greene, "An analysis of transfer in gas-shielded welding arcs," *Transactions of the American Institute of Electrical Engineers, Part II: Applications and Industry*, vol. 79, no. 3, pp. 194–203, 1960. 6, 8, 11

[26] J. C. Amson, "Lorentz force in the molten tip of an arc electrode," *British Journal of Applied Physics*, vol. 16, no. 8, pp. 1169–1179, 1965. 6, 8, 9, 10, 11

[27] L. F. N. Marques, E. B. F. Santos, A. P. Gerlich, and E. M. Braga, "Fatigue life assessment of weld joints manufactured by GMAW and CW-GMAW processes," *Science and Technology of Welding and Joining*, vol. 22, pp. 87–96, feb 2017. 6

[28] E. S. Costa, P. D. C. Assunção, E. B. F. Dos Santos, L. G. Feio, M. S. Q. Bittencourt, and E. M. Braga, "Residual stresses in cold-wire gas metal arc welding," *Science and Technology of Welding and Joining*, pp. 1–8, mar 2017.

[29] P. D. C. Assunção, R. A. Ribeiro, E. B. F. Dos Santos, A. P. Gerlich, and E. M. Braga, "Feasibility of narrow gap welding using the cold-wire gas metal arc welding (CW-GMAW) process," *Welding in the World*, pp. 1–7, 2017. 6

[30] J. N. Dupont and A. R. Marder, "Thermal Efficiency of Arc Welding Processes," *Welding Journal*, no. December, pp. 406s–416s, 1995. 7

[31] J. Hu and H. Tsai, "Heat and mass transfer in gas metal arc welding. Part I: The arc," *International Journal of Heat and Mass Transfer*, vol. 50, pp. 833–846, mar 2007. 7, 45, 52

[32] J. Hu and H. Tsai, "Heat and mass transfer in gas metal arc welding. Part II: The metal," *International Journal of Heat and Mass Transfer*, vol. 50, pp. 808–820, mar 2007. 8, 46

[33] V. K. Goyal, P. K. Ghosh, and J. S. Saini, "Analytical studies on thermal behaviour and geometry of weld pool in pulsed current gas metal arc welding," *Journal of Materials Processing Technology*, vol. 209, no. 3, pp. 1318–1336, 2009. 7

[34] F. Lu, H.-P. Wang, A. B. Murphy, and B. E. Carlson, "Analysis of energy flow in gas metal arc welding processes through self-consistent three-dimensional process simulation," *International Journal of Heat and Mass Transfer*, vol. 68, no. JANUARY 2014, pp. 215–223, 2014. 7

[35] A. Haelsig, M. Kusch, and P. Mayr, "Calorimetric analyses of the comprehensive heat flow for gas metal arc welding," *Welding in the World*, vol. 59, pp. 191–199, mar 2015.

[36] E. J. Soderstrom, K. M. Scott, and P. F. Mendez, "Calorimetric Measurement of Droplet Temperature in GMAW," *Welding Journal*, vol. 90, no. 4, pp. 77S–84S, 2011. 59

[37] C. McIntosh, J. Chapuis, and P. Mendez, "Effect of Ar-CO2 Gas Blends on Droplet Temperature in GMAW," *Welding Journal*, vol. 95, no. August, pp. 273s–279s, 2016. 7, 59

[38] S. Rhee and E. Kannatey-Asibu., "Observation of metal transfer during gas metal arc welding," *Welding journal*, vol. 71, no. 10, pp. 381S–386S, 1992. 7, 11, 12, 22

[39] Y. S. Kim and T. W. Eagar, "Analysis of metal transfer in gas metal arc welding," *Welding Journal*, vol. 72, pp. 269s–278s, jun 1993. 11, 12

[40] Y. S. Kim and T. W. Eagar, "Metal Transfer in Pulsed Current Gas Metal Arc Welding," *Welding Journal*, vol. 72, no. July, pp. 279–287, 1993. 13, 22

[41] P. R. Heald, R. B. Madican, T. A. Siewert, and S. Liu, "Mapping the Droplet Transfer Modes for an Er100s-1 Gmaw Electrode," *Welding Journal*, vol. 73, no. 2, pp. S38–S44, 1994.

[42] L. L. Wang, F. G. Lu, H. P. Wang, A. B. Murphy, and X. H. Tang, "Effects of shielding gas composition on arc profile and molten pool dynamics in gas metal arc welding of steels," *Journal of Physics D: Applied Physics*, vol. 47, p. 465202, nov 2014.

[43] K. Pal and S. K. Pal, "Effect of pulse parameters on weld quality in pulsed gas metal arc welding: A review," *Journal of Materials Engineering and Performance*, vol. 20, no. 6, pp. 918–931, 2011. 7

[44] M. Hertel, A. Spille-Kohoff, U. Füssel, and M. Schnick, "Numerical simulation of droplet detachment in pulsed gasmetal arc welding including the influence of metal vapour," *Journal of Physics D: Applied Physics*, vol. 46, p. 224003, jun 2013. 8, 15, 16, 35, 44, 45, 52

[45] N. Arif, J. H. Lee, and C. D. Yoo, "Forcedisplacement model for analysis of pulsed-GMAW," *Journal of Physics D: Applied Physics*, vol. 42, no. 3, p. 035504, 2009. 9, 45

[46] J. F. Lancaster, *The Physics of Welding*. Oxford: Pregamon Press., 2 edition ed., 1986. 9, 10

[47] S. Rhee and E. Kannatey-Asibu, "Analysis of arc pressure effect on metal transfer in gas-metal arc welding," *Journal of Applied Physics*, vol. 70, pp. 5068–5075, nov 1991. 10, 12

[48] J. Haidar, "The dynamic effects of metal vapour in gas metal arc welding," *Journal of Physics D: Applied Physics*, vol. 43, no. 16, p. 165204, 2010. 10, 15, 50

[49] L. a. Jones, T. W. Eagar, and J. H. Lang, "A dynamic model of drops detaching from a gas metal arc welding electrode," *Journal of Physics D: Applied Physics*, vol. 31, no. 1, pp. 107–123, 1999. 10

[50] A. Scotti, V. Ponomarev, and W. Lucas, "A scientific application oriented classification for metal transfer modes in GMA welding," *Journal of Materials Processing Technology*, vol. 212, pp. 1406–1413, jun 2012. 11, 12, 68, 69

[51] A. Scotti, V. Ponomarev, and W. Lucas, "Interchangeable metal transfer phenomenon in GMA welding: Features, mechanisms, classification," *Journal of Materials Processing Technology*, vol. 214, pp. 2488–2496, nov 2014. 11, 68, 69

[52] S. J. Bless, "Drop transfer in short-circuit welding," *Journal of Physics D: Applied Physics*, vol. 7, pp. 526–539, 1974. 11

[53] C.-s. Wu, D.-g. Zou, and J.-q. Gao, "Determining the critical transition current for metal transfer in gas metal arc welding (GMAW)," *Frontiers of Materials Science in China*, vol. 2, pp. 397–401, dec 2008. 12

[54] J. J. Lowke, "Physical basis for the transition from globular to spray modes in gas metal arc welding," *Journal of Physics D: Applied Physics*, vol. 42, p. 135204, jul 2009. 12

[55] N. T. Jenkins, P. F. Mendez, and T. W. Eagar, "Effect of Arc Welding Electrode Temperature on Vapor and Fume Composition," in *Trends in Welding Research, Proceedings of the 7th International Conference*, no. 2, pp. 491–496, 2005. 12

[56] R. Li, J. Yue, R. Sun, G. Mi, C. Wang, and X. Shao, "A study of droplet transfer behavior in ultra-narrow gap laser arc hybrid welding," *The International Journal of Advanced Manufacturing Technology*, vol. 87, pp. 2997–3008, dec 2016. 12

[57] P. Praveen, P. Yarlagadda, and M. Kang, "Advancements in pulse gas metal arc welding," *Journal of Materials Processing Technology*, vol. 164-165, pp. 1113–1119, 2005. 13

[58] P. Palani and N. Murugan, "Selection of parameters of pulsed current gas metal arc welding," *Journal of Materials Processing Technology*, vol. 172, pp. 1–10, feb 2006. 13

[59] C. S. Wu, M. a. Chen, and Y. F. Lu, "Effect of current waveforms on metal transfer in pulsed gas metal arc welding," *Measurement Science and Technology*, vol. 16, pp. 2459–2465, dec 2005. 13, 22

[60] S. Zielinska, K. Musioł, K. Dzierżęga, S. Pellerin, F. Valensi, C. de Izarra, and F. Briand, "Investigations of GMAW plasma by optical emission spectroscopy," *Plasma Sources Science and Technology*, vol. 16, no. 4, pp. 832–838, 2007. 14, 15, 17

[61] M. Schnick, U. Füssel, M. Hertel, a. Spille-Kohoff, and a. B. Murphy, "Metal vapour causes a central minimum in arc temperature in gasmetal arc welding through increased radiative emission," *Journal of Physics D: Applied Physics*, vol. 43, p. 022001, 2009. 15, 35

[62] F. Valensi, S. Pellerin, A. Boutaghane, K. Dzierzega, S. Zielinska, N. Pellerin, and F. Briand, "Plasma diagnostics in gas metal arc welding by optical emission spectroscopy," *Journal of Physics D: Applied Physics*, vol. 43, p. 434002, nov 2010. 16

[63] M. Schnick, U. Fuessel, M. Hertel, M. Haessler, A. Spille-Kohoff, and a. B. Murphy, "Modelling of gasmetal arc welding taking into account metal vapour," *Journal of Physics D: Applied Physics*, vol. 43, p. 434008, nov 2010. 15, 41

[64] M. Schnick, U. Fuessel, M. Hertel, A. Spille-Kohoff, and A. B. Murphy, "Numerical investigations of arc behaviour in gas metal arc welding using ANSYS CFX," *Frontiers of Materials Science*, vol. 5, no. 2, pp. 98–108, 2011. 15, 16

[65] M. Schnick, M. Hertel, U. Fuessel, and D. Uhrlandt, "Energy balance in MIG arcs," *Journal of Physics D: Applied Physics*, vol. 46, p. 224002, jun 2013. 15

[66] M. Boselli, V. Colombo, E. Ghedini, M. Gherardi, and P. Sanibondi, "Dynamic analysis of droplet transfer in gasmetal arc welding: modelling and experiments," *Plasma Sources Science and Technology*, vol. 21, no. 5, p. 055015, 2012. 15, 16, 35, 36, 41

[67] R. Kozakov, G. Gött, H. Schöpp, D. Uhrlandt, M. Schnick, M. Häßler, U. Füssel, and S. Rose, "Spatial structure of the arc in a pulsed GMAW process," *Journal of Physics D: Applied Physics*, vol. 46, no. 22, p. 224001, 2013.

[68] M. Boselli, V. Colombo, E. Ghedini, M. Gherardi, and P. Sanibondi, "Two-dimensional time-dependent modelling of fume formation in a pulsed gas metal arc welding process," *Journal of Physics D: Applied Physics*, vol. 46, p. 224006, jun 2013. 15, 16, 35

[69] M. Hertel, S. Rose, and U. Füssel, "Numerical simulation of arc and droplet transfer in pulsed GMAW of mild steel in argon," *Welding in the World*, vol. 60, pp. 1055–1061, sep 2016. 15, 16, 35, 44

[70] G. Wilhelm, R. Kozakov, G. Gött, H. Schöpp, and D. Uhrlandt, "Behaviour of the iron vapour core in the arc of a controlled short-arc GMAW process with different shielding gases," *Journal of Physics D: Applied Physics*, vol. 45, no. 8, p. 085202, 2012. 15

[71] A. B. Murphy, "The effects of metal vapour in arc welding," *Journal of Physics D: Applied Physics*, vol. 43, no. 16, p. 165204, 2010. 15, 16, 35, 41, 50

[72] F. Valensi, S. Pellerin, Q. Castillon, A. Boutaghane, K. Dzierzega, S. Zielinska, N. Pellerin, and F. Briand, "Study of the spray to globular transition in gas metal arc welding: a spectroscopic investigation," *Journal of Physics D: Applied Physics*, vol. 46, p. 224005, 2013. 16

[73] Q. Lin, X. Li, and S. W. Simpson, "Metal transfer measurements in gas metal arc welding," *Journal of Physics D: Applied Physics*, vol. 34, pp. 347–353, feb 2001. 22

[74] S. Kumar and S. C. Bhaduri, "Theoretical Investigation of Penetration Characteristics in Gas Metal-Arc Welding Using Finite Element Method," vol. 26, no. June, pp. 611–624, 1995. 22

[75] C. H. Kim, W. Zhang, and T. DebRoy, "Modeling of temperature field and solidified surface profile during gas-metal arc fillet welding," *Journal of Applied Physics*, vol. 94, no. 4, pp. 2667–2679, 2003. 22

[76] J. Hu, H. Guo, and H. L. Tsai, "Weld pool dynamics and the formation of ripples in 3D gas metal arc welding," *International Journal of Heat and Mass Transfer*, vol. 51, no. 9-10, pp. 2537–2552, 2008. 22, 30

[77] S. K. Choi, C. D. Yoo, and Y.-s. Kim, "The dynamic analysis of metal transfer in pulsed current gas metal arc welding," *Journal of Physics D: Applied Physics*, vol. 31, pp. 207–215, jan 1998. 22

[78] P. K. Ghosh, L. Dorn, K. Devakumaran, and F. Hofmann, "Pulsed Current Gas Metal Arc Welding under Different Shielding and Pulse Parameters; Part 1: Arc Characteristics," *ISIJ International*, vol. 49, no. 2, pp. 251–260, 2009. 22

[79] B. Y. B. Yudodibroto, M. J. M. Hermans, G. Ouden, and I. M. Richardson, "Observations on Droplet and Arc Behaviour during Pulsed GMAW," *Welding in the World*, vol. 53, no. 7-8, pp. R171–R180, 2013. 22

[80] G. Nave, S. Johansson, R. C. M. Learner, A. P. Thorne, and J. W. Brault, "A new multiplet table for Fe I," *The Astrophysical Journal Supplement Series*, vol. 94, p. 221, aug 1994. 23, 33

[81] S. Yamashita, A. Fujinaga, M. Yamamoto, K. Shinozaki, K. Kadoi, K. Mitsui, and H. Usui, "In-situ Temperature Measurement using Monochrome High-speed Sensors during Laser Welding," *Quarterly Journal of the Japan Welding Society*, vol. 31, no. 4, pp. 78s–81s, 2013.

[82] A. Kramida, Y. Ralchenko, J. Reader, and N. A. Team, "NIST Atomic Spectra Database (ver. 5.3)." NIST Atomic Spectra Database (ver. 5.3), [Online]. Available:

{\tt{http://physics.nist.gov/asd}} [2017, February 10]. National Institute of Standards and Technology, Gaithersburg, MD., 2015. 23

[83] W. Rasband, "ImageJ 1.50b - Imaging Processing and Analysis in Java," 2015. 26

[84] M. Hall, E. Frank, G. Holmes, B. Pfahringer, P. Reutemann, and I. H. Witten, "The WEKA data mining software," *ACM SIGKDD Explorations Newsletter*, vol. 11, p. 10, nov 2009. 27

[85] L. Breiman and P. Spector, "Submodel Selection and Evaluation in Regression. The X-Random Case," *International Statistical Review / Revue Internationale de Statistique*, vol. 60, p. 291, dec 1992. 28, 54

[86] P. Zhang, "Model Selection Via Multifold Cross Validation," *The Annals of Statistics*, vol. 21, no. 1, pp. 299–313, 1993. 28, 54

[87] J. Liu, Z. Rao, S. Liao, and H. Tsai, "Numerical investigation of weld pool behaviors and ripple formation for a moving GTA welding under pulsed currents," *International Journal of Heat and Mass Transfer*, vol. 91, pp. 990–1000, 2015. 30

[88] J. Haidar and J. J. Lowke, "Predictions of metal droplet formation in arc welding," *Journal of Physics D: Applied Physics*, vol. 29, pp. 2951–2960, dec 1996. 45, 52

[89] F. Wang, W. K. Hou, W. K. Hou, S. J. Hu, E. Kannatey-Asibu, W. W. Schultz, and P. C. Wang, "Modelling and analysis of metal transfer in gas metal arc welding," *J. Physics D.:Applied Physics*, vol. 36, pp. 1143–1152, 2003. 45, 52

[90] Z. H. Rao, J. Zhou, and H. L. Tsai, "Determination of equilibrium wire-feed-speeds for stable gas metal arc welding," *International Journal of Heat and Mass Transfer*, vol. 55, no. 23-24, pp. 6651–6664, 2012. 45, 52

[91] G. Xu, J. Hu, and H. Tsai, "Three-dimensional modeling of arc plasma and metal transfer in gas metal arc welding," *International Journal of Heat and Mass Transfer*, vol. 52, pp. 1709–1724, mar 2009. 46

[92] G. I. Barenblatt, *Dimensional analysis*. Gordon & Breach Publishing Group, 1st ed., 1987. 50, 85

[93] E. Siewert, J. Schein, and G. Forster, "Determination of enthalpy, temperature, surface tension and geometry of the material transfer in PGMAW for the system argoniron," *Journal of Physics D: Applied Physics*, vol. 46, no. 22, p. 224008, 2013. 50

[94] S. Arlot and A. Celisse, "A survey of cross-validation procedures for model selection," *Statistics Surveys*, vol. 4, pp. 40–79, 2010. 54

[95] S. Borra and A. Di Ciaccio, "Measuring the prediction error. A comparison of cross-validation, bootstrap and covariance penalty methods," *Computational Statistics and Data Analysis*, vol. 54, no. 12, pp. 2976–2989, 2010. 54

[96] D. Giavarina, "Understanding Bland Altman analysis," *Biochemia Medica*, vol. 25, no. 2, pp. 141–151, 2015. 55

[97] T. Beltrame, R. Amelard, R. Villar, M. J. Shafiee, A. Wong, and R. L. Hughson, "Estimating oxygen uptake and energy expenditure during treadmill walking by neural network analysis of easy-to-obtain inputs," *Journal of Applied Physiology*, vol. 121, pp. 1226–1233, nov 2016. 57

APPENDICES

Appendix A

Determination of dimensionless groups

The theory of dimensional analysis states that if a physical phenomenon is a function of n independent variables, then its dimensionless quantity is equal to a function of $n - k$ dimensionless variables, being k the number of fundamental units [92]. Say a is the dependent variable and a_1, a_2,...,a_n are the independent variables, then it follow that

$$a = f\left(a_1, a_2, \ldots, a_n\right) \tag{A.1}$$

which in terms of dimensionless variables is equivalent to say that

$$\bar{a} = \psi\left(\bar{a}_1, \bar{a}_2, \ldots, \bar{a}_{n-k}\right) \tag{A.2}$$

where $(\bar{a}_1)$ represents the dimensionless quantity of the variable a_1. This is formally know as the Buckingham π-theorem.

As discussed in sections 2.2.1 and 5.1.3, the process parameters and physical properties identified to have an influence in the droplet velocity are:

$I_p =$ peak current $[I]$;

$I_b =$ background current $[I]$;

$I_m =$ mean current $[I]$;

$V =$ average voltage $[ML^2T^{-3}I^{-1}]$;

$t_p =$ time at peak current $[T]$;

$f =$ pulse frequency $[T^{-1}]$;

$s =$ wire feeding speed $[LT^{-1}]$;

$\mu_o =$ permeability constant $[MLT^{-2}I^{-2}]$;

$\sigma =$ arc electrical conductivity $[M^{-1}L^{-3}T^3I^2]$;

$\rho =$ wire density $[ML^{-3}]$;

$\gamma =$ surface tension coefficient $[MT^{-2}]$;

$r =$ droplet radius $[L]$.

Being the droplet velocity, v, the dependent variable, this gives a total of twelve independent variables plus the dependent variable droplet speed, giving a total of thirteen variable, $n = 13$. The number of fundamental units involved in this problem are four, $k = 4$: length $[L]$, mass $[M]$, time $[T]$ and current $[I]$. Therefore, according to the Buckingham π-theorem, there should be nine dimensionless numbers, amongst which eight are independent and the ninth is the dimensionless values of velocity.

The procedure used to find the dimensionless groups was as follow. First, the fundamental dimensions were expressed in term of the independent variables as follow:

$$L = [r] \tag{A.3}$$

$$I = [I_p] \tag{A.4}$$

$$T = \left[\frac{r}{s}\right] \tag{A.5}$$

$$M = \gamma \left(\frac{r}{s}\right)^2 \tag{A.6}$$

Second, each of the variables were multiplied by the reciprocal of their fundamental units using the fundamental units (length $[L]$, mass $[M]$, time $[T]$ and current $[I]$) as expressed in Eq. A.3 to A.6.

It follows that, background current, which in fundamental units is $[I]$, has to be multiplied by the reciprocal of current from Eq. A.4, yielding $\bar{I_b}$ as follow

$$\bar{I_b} = I_b \left[I^{-1}\right] = \frac{I_b}{I_p} \tag{A.7}$$

Similarly, the dimensionless welding mean current, $\bar{I_m}$ current is equal to

$$\bar{I_m} = I_m \left[I^{-1}\right] = \frac{I_m}{I_p} \tag{A.8}$$

The average voltage, which in fundamental units is $[ML^2T^{-3}I^{-1}]$, if multiplied by the reciprocal of its fundamental dimensions yield the dimensionless voltage, $\bar{V}$ as

$$\begin{aligned} \bar{V} &= V \left[M^{-1}L^{-2}T^3I^1\right] \\ &= V \frac{1}{\gamma \left(\frac{r}{s}\right)^2} \frac{1}{r^{-2}} \left(\frac{r}{s}\right)^3 I_p \\ &= \frac{I_p V}{\gamma s r} \end{aligned} \tag{A.9}$$

Peak time, which in fundamental units is $[T]$, has to be multiplied by the reciprocal of time Eq. A.5 yielding

$$\bar{t_p} = t_p \left[T^{-1}\right] = t_p \frac{s}{r} \tag{A.10}$$

Similarly, the dimensionless pulse frequency, $\bar{f}$, is found by multiplying pulse by the reciprocal of time, as expressed in Eq. A.5.

$$\bar{f} = f \left[T^1\right] = f \frac{r}{s} \tag{A.11}$$

The dimensionless permeability of free space, $\bar{\mu_0}$, is found by multiplying μ_0 by the

reciprocal of its fundamental dimensions

$$\begin{aligned}\bar{\mu_0} &= \mu_0 \left[M^{-1}L^{-1}T^2I^2\right] \\ &= \mu_0 \frac{1}{\gamma \left(\frac{r}{s}\right)^2} \frac{1}{r} \left(\frac{r}{s}\right)^2 I_p^2 \\ &= \frac{\mu_0 I_p^2}{\gamma r}\end{aligned} \tag{A.12}$$

Likewise, the dimensionless electrical conductivity of the arc, $\bar{\sigma}$, is found by multiplying σ by the reciprocal of its fundamental dimensions

$$\begin{aligned}\bar{\sigma} &= \sigma \left[M^1L^3T^{-3}I^{-2}\right] \\ &= \sigma\gamma \left(\frac{r}{s}\right)^2 r^3 \left(\frac{s}{r}\right)^3 \frac{1}{I_p^2} \\ &= \frac{\sigma\gamma s r^2}{I_p^2}\end{aligned} \tag{A.13}$$

The wire density is expressed as

$$\begin{aligned}\bar{\rho} &= \rho \left[M^{-1}L^3\right] \\ &= \rho \frac{1}{\gamma \left(\frac{r}{s}\right)^2} r^3 \\ &= \frac{\rho r s^2}{\gamma}\end{aligned} \tag{A.14}$$

Lastly, the dimensionless droplet velocity, which in fundamental units is $[LT^{-1}]$, can be assumed as has to be multiplied by the reciprocal of its fundamental dimensions

$$\begin{aligned}\bar{v} &= v \left[L^{-1}T^1\right] \\ &= v \frac{1}{r} \frac{r}{s} \\ &= \frac{v}{s}\end{aligned} \tag{A.15}$$

The dimensionless droplet velocity as expressed in Eq. A.15 can also be expressed as in Eq. A.16. The model using the $\bar{v}$ as in Eq. A.16 would predict droplet velocity values closer to the measured ones.

$$\bar{v} = \sqrt{\frac{v}{s}} \tag{A.16}$$

Therefore, those are the nine dimensionless groups used for the prediction of droplet speed presented in section 5.1.4. The dimensionless values of peak current, droplet radius, wire feeding speed and surface tension are not shown because they all yield to 1, when the procedure is applied to them.

Appendix B

Neural network training procedure

To find a model of high predictability, in this work measured by the Pearson correlation coefficient values, the NN algorithm parameters were varied such that the highest possible Pearson correlation coefficient were achieved. Varying the algorithm parameters, it was verified that the number of hidden nodes in the hidden layer and the number of cross validation folds used affects more strongly the correlation coefficient.

In Fig. B.1 the correlation coefficient is plotted against the number of hidden nodes for various number of cross-validation folds. One can notice that regardless of the number cross-validation folds used, as the hidden nodes are increased, the correlation coefficient decreases. Hence the number of hidden nodes in the hidden layer was was chosen as one, given that would give the highest correlation coefficient.

Next, the number of cross-validation folds was varied, for 1 to 4 hidden nodes, and the result is shown in Fig. B.2. From this figure one can see that, using only one hidden node leads to highest correlation coefficient, and that as the number of cross-validation folds increase, the correlation coefficient value approaches to a constant value. At 10 cross-validation folds and 1 hidden node, the correlation coefficient if equal to 0.8971 and 0.9112 for models 1 and 2, respectively.

Based on this methodology, the neural network was trained having one hidden node and 10 cross validation folds. The remaining NN parameters were: ridge equal to 0.01,

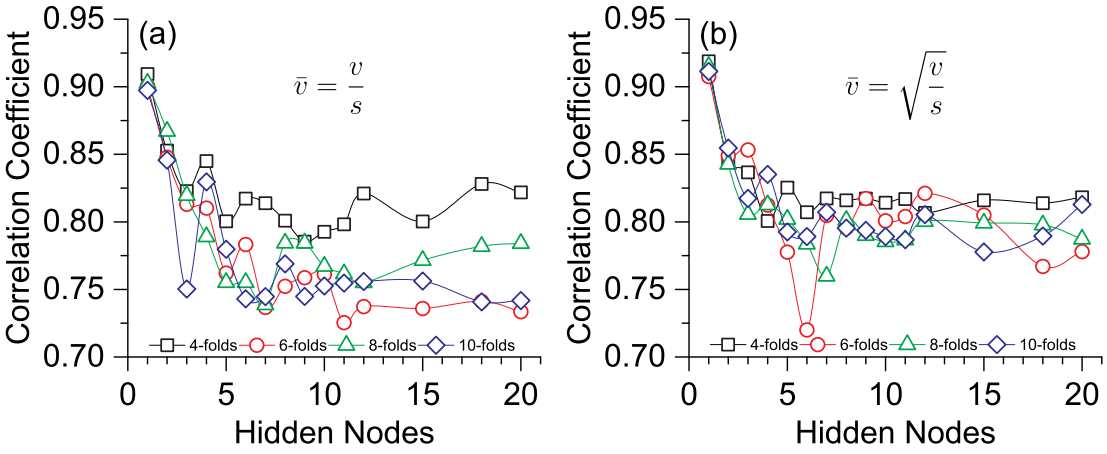

Figure B.1: Variation of Pearson correlation coefficient as a function of the number of hidden nodes in the the hidden layer: (a) for model, $\bar{v} = v/s$, and (b) for model 2, $\bar{v} = \sqrt{v/s}$.

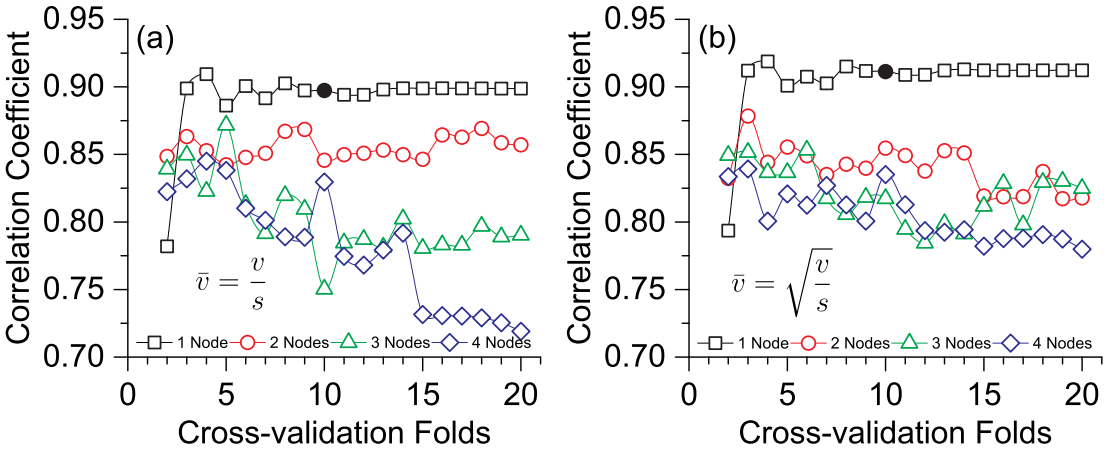

Figure B.2: Variation of Pearson correlation coefficient as a function of the number of cross-validation folds: (a) for model, $\bar{v} = v/s$, and (b) for model 2, $\bar{v} = \sqrt{v/s}$. The condition used used to train the NN for predicting the droplet velocity is indicated by the filled circle, •.

seed equal to 1 and tolerance of 10^{-6}.